

**Measuring the Local ISM Along the
Sight Lines of the Two *Voyager*
Spacecraft with *HST*/STIS**

by

Julia R. Zachary
Class of 2017

A thesis submitted to the
faculty of Wesleyan University
in partial fulfillment of the requirements for the
Degree of Bachelor of Arts
with Departmental Honors in Astronomy

Look again at that dot. That's here. That's home. That's us. On it everyone you love, everyone you know, everyone you ever heard of, every human being who ever was, lived out their lives. The aggregate of our joy and suffering, thousands of confident religions, ideologies, and economic doctrines, every hunter and forager, every hero and coward, every creator and destroyer of civilization, every king and peasant, every young couple in love, every mother and father, hopeful child, inventor and explorer, every teacher of morals, every corrupt politician, every "superstar," every "supreme leader," every saint and sinner in the history of our species lived there—on a mote of dust suspended in a sunbeam.

—CARL SAGAN

Pale Blue Dot: A Vision of Human Future in Space

Acknowledgements

First and foremost, I want to thank my adviser, Seth Redfield, who tirelessly and unfailingly answered all my many questions. Without your guidance and knowledge, I would've never done this research and written this thesis.

Thank you to professors whose advice or input I sought over the course of this year: Meredith Hughes, Ed Moran, Christina Othon, and Roy Kilgard. I'm always grateful for when you take time out of your day to talk with me.

My fellow thesisers: JD, GD, SW. It's been a loooooong road, from starting off together in 155 to now finishing our senior theses. Glad I did it with you guys.

To CE, CW, AH, AR, AW, NS, and MS: You are all some of my very best friends at Wes. It's been quite the adventure!

To JKS, KMM: I am so glad I've been able to spend my whole life with you as my friends.

To the physics crew: It's been a wild ride. Thank you for working on/struggling through homework with me for four years.

Of course, to my family: Thank you for letting me talk your ears off about astronomy for the last four years. Thank you for your constant love and support. I love you.

Contents

| | | |
|----------|---|-----------|
| 1 | Introduction | 1 |
| 1.1 | <i>Voyager</i> | 1 |
| 1.2 | The Structure of the Heliosphere | 5 |
| 1.2.1 | Interplanetary Magnetic Fields | 6 |
| 1.2.2 | Heliospheric Termination Shock | 7 |
| 1.2.3 | The Heliosheath, Heliopause, and Beyond | 8 |
| 1.3 | The Nature of the Interstellar Medium | 11 |
| 1.3.1 | Interstellar Magnetic Fields | 13 |
| 1.3.2 | Gas Clouds | 14 |
| 1.3.3 | Dust Grains | 15 |
| 1.3.4 | Kinematic Structure | 16 |
| 1.4 | <i>Hubble Space Telescope</i> | 18 |
| 1.5 | Connections to <i>Voyager</i> | 20 |
| 2 | Observations and Data Reduction | 21 |
| 2.1 | Space Telescope Imaging Spectrograph | 21 |
| 2.2 | Observations | 22 |
| 2.3 | Data Reduction | 25 |
| 2.4 | Target Stars | 26 |

| | | |
|----------|--|-----------|
| 3 | Fitting and Results | 28 |
| 3.1 | Interstellar Ions | 28 |
| 3.2 | The Fitting Procedure | 30 |
| 3.2.1 | Continuum | 30 |
| 3.2.2 | ISM Absorption | 32 |
| 3.2.3 | Error Analysis | 34 |
| 3.3 | Fits | 35 |
| 3.4 | Fit Parameters | 41 |
| 3.4.1 | Velocity Offsets | 43 |
| 3.4.2 | Geocoronal Features | 44 |
| 3.5 | The Lyman α Profile | 49 |
| 4 | Analysis of Physical Parameters | 53 |
| 4.1 | Comparing with the Kinematic Model | 53 |
| 4.1.1 | The <i>Voyager 1</i> Sight Line | 55 |
| 4.1.2 | The <i>Voyager 2</i> Sight Line | 56 |
| 4.2 | Temperature and Turbulence | 58 |
| 4.3 | Abundance and Depletion | 64 |
| 4.4 | Electron Density | 67 |
| 4.4.1 | Comparisons to <i>Voyager</i> | 70 |
| 5 | Conclusions and Future Work | 73 |
| 5.1 | Future Work | 74 |
| 5.2 | The “Interstellar Road Map” | 78 |
| | Bibliography | 82 |

Chapter 1

Introduction

The general purpose of this thesis is to explore the structure and composition of the local interstellar medium using *Hubble Space Telescope* spectra coupled with in situ *Voyager* observations. In order to discuss the importance of the analysis that will be subsequently presented, I will first introduce the various components of my research, including the spacecraft and telescope, as well as the structural components of the heliosphere and interstellar medium. The following chapter provides an overview and background to the entire project to allow for a complete introduction to the topic of the interstellar medium. Many interstellar medium observations have been taken with the *Hubble Space Telescope*, but never before have those observations been combined with data from a spacecraft actually in the interstellar medium. The *Voyager* spacecraft represent a new frontier in interstellar medium research, presenting the first ever in situ interstellar observations.

1.1 *Voyager*

On September 5, 1977, the *Voyager 1* spacecraft was launched from the NASA Kennedy Space Center at Cape Canaveral, Florida. *Voyager 1* and its counterpart, *Voyager 2*, which was launched a month earlier, were to study the interplanetary space between Earth and Saturn, explore the Saturnian and Jovian planetary systems, and, if possible, extend the mission to Uranus and Neptune (Kohlhase &

Penzo 1977). The mission was conceived out of the idea for a “grand tour” of the outer Solar System. This grand tour was initiated due to a fortuitous planetary alignment, and *Voyager 2* was able to travel to all four giant planets (Sagan 1994; Rudd et al. 1997). *Voyager 1*’s slightly-less grand tour included traveling to Jupiter, Saturn, and Titan, one of the largest of the Saturnian moons. By the end of 1989, it was clear that both spacecraft were heading on separate paths out of the ecliptic plane. *Voyager 1* was headed north after being boosted by Saturn, and *Voyager 2* was headed south after its encounter with Neptune at an angle nearly perpendicular to *Voyager 1* (Rudd et al. 1997). An extension of the original *Voyager* mission, the Voyager Interstellar Mission (VIM) intended to not only continue investigating the interplanetary medium, but also to characterize the structure of the heliosphere and begin studying the interstellar medium (Rudd et al. 1997). The next year, at Carl Sagan’s request, *Voyager 1* turned its camera back around towards the Earth one last time, taking the now infamous “Pale Blue Dot” image, reproduced in Figure 1.1 (Sagan 1994).

The spacecraft have spent the last twenty-five years traveling to the outer edges of the Solar System. In 1998, *Voyager 1* passed *Pioneer 10* to become the most distant man-made object in space (Stone et al. 2014). Like *Pioneer 10*, the *Voyager* spacecraft are powered by plutonium oxide radioisotope thermoelectric generators (RTGs). However, while *Pioneer 10* was powered by four SNAP-19 RTGs delivering 165 W of power, the *Voyagers* were (and are) powered by three multihundred-watt (MHW) RTGs (Furlong & Wahlquist 1999). The MHW RTGs relied on a new heat source: 24 pressed PuO₂ fuel spheres, and produced close to 450 W of power. The RTGs on the *Voyager* spacecraft will eventually fully decay sometime after 2025 (Kohlhase & Penzo 1977). After they lose their power, the *Voyagers* will drift through interstellar space, reaching the Oort Cloud in 300

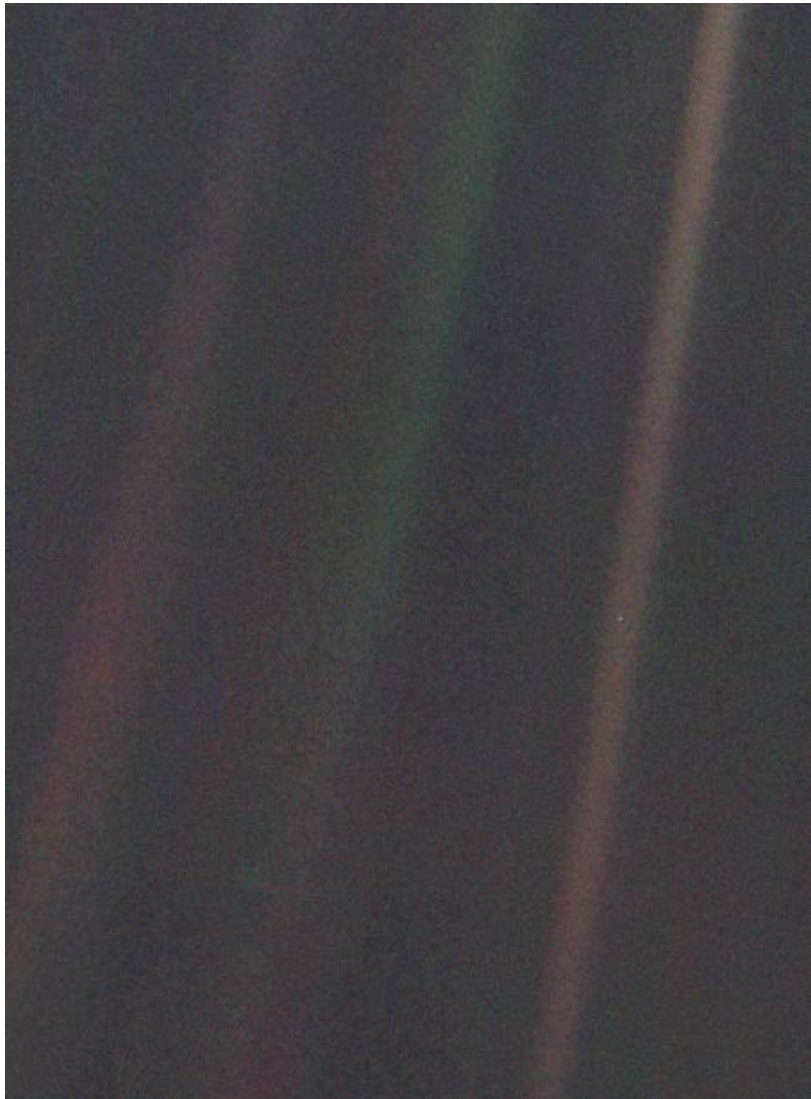


Figure 1.1: Taken by *Voyager 1* in 1990, this image shows Earth as it looked from 4 billion miles away. At this distance, Earth is just a tiny point of light just over a tenth of a pixel in size (seen in the center-right of this image).

years, with *Voyager 2* passing by Sirius in $\sim 300,000$ years (Rudd et al. 1997).

Out of the eleven scientific instruments originally operational on the Voyagers, only five are currently still operational (Rudd et al. 1997). These instruments are now crucial to providing insight into the composition, structure, and presence of the various components of the heliosphere and interstellar space. One of the most important instruments is the Cosmic Ray Subsystem (CRS), which uses three independent solid state detector telescopes to take direct measurements of galactic cosmic ray intensities (Stone et al. 1977). These telescopes allow for the detection and measurement of low-energy galactic cosmic rays, which provide information about particle acceleration and interstellar propagation (Stone et al. 1977). The Low Energy Charged Particle (LECP) experiments involve using two detectors on each spacecraft to measure the differential in energy fluxes and angular distributions of both ions and electrons (Krimigis et al. 1977). The magnetometers on-board the *Voyagers* provide measurements of the magnetic fields of both planetary and interplanetary media, which are crucial to understanding the structure of the heliosphere. Other still functioning instruments include the ultraviolet spectrometer and the Plasma Wave System (PLS). Since basic planetary dynamical processes are often associated with wave-particle interactions, the PLS provides an understanding of these processes by measuring electric field components between 10 Hz–56 kHz (Scarf & Gurnett 1977).

On August 25, 2012, the Voyager Interstellar Mission team received direct confirmation that *Voyager 1* had entered interstellar space (Gurnett et al. 2013). It is expected that *Voyager 2* will exit the heliosphere within the next couple of years (Stone et al. 2014). For the first time, humans have sent a spacecraft outside the confines of the Solar System, which for thousands of years seemed to be the boundary of the known universe. As of April 19, 2017, *Voyager 1* is in

interstellar space at a distance of 137.73 AU from Earth, and *Voyager 2* is in the heliosheath at 114.0 AU from Earth.¹ The two spacecraft are the fastest-moving human-made objects, travelling at 3.6 AU/year and 3.3 AU/year, respectively (Stone et al. 2005).

1.2 The Structure of the Heliosphere

The volume of interplanetary space through which the *Voyagers* have spent much of their mission traveling is known as the heliosphere. It can be thought of as a giant bubble enclosing the Sun and planets, protecting the Solar System from high energy cosmic rays. This bubble is formed by the solar wind coming into contact with the gas and magnetic fields of the interstellar medium (Mewaldt & Liewer 2000). The solar wind is actually plasma emanating from the Sun at speeds of 400–700 km s⁻¹ (Stone et al. 2014). The heliosphere not only shields the Solar System from cosmic rays, but also guards against interstellar plasma, fields, and dust (Mewaldt & Liewer 2000). Because the heliosphere is moving with respect to the interstellar medium, its shape is affected by pressure dynamics. In the upwind direction, there is a compressed “nose,” and conversely, a downwind “tail” (McComas et al. 2012).

As the solar wind moves out from the Sun, it eventually comes into contact with much cooler interstellar plasma, creating a boundary known as the heliopause (Gurnett et al. 2013). The heliopause is considered to be the edge of the heliosphere (Stone et al. 2014). It takes up to a year for the solar wind to reach the outer edges of the heliosphere, during which the wind evolves significantly over such large distances. Coronal mass ejections overtake the slower solar wind, pro-

¹<http://voyager.jpl.nasa.gov/where/index.html>

ducing compressed regions known as merged interaction regions (MIRs). MIRs are associated with enhanced magnetic field magnitudes and fluctuations, and can also be related to shocks in the solar wind, where speeds can increase or decrease rapidly (Richardson et al. 2008).

1.2.1 Interplanetary Magnetic Fields

As seen in Figure 1.2, the interplanetary and solar magnetic fields are carried by the solar wind, forming a spiral structure. This structure has origins in the coronal magnetic field, which is driven by the motion of plasma in the photosphere of the Sun (Owens & Forsyth 2013). The magnetic field lines of the heliosphere are fixed in the photosphere, rotating with the Sun. Because the magnetic field lines remain “frozen,” the rotation causes twisting, forcing the field into a spiral (Parker 1958; Owens & Forsyth 2013). Once the solar wind achieves supersonic speeds, it drags the plasma out into the heliosphere, forming the heliospheric magnetic field. In addition to the supersonic solar wind, there is a belt of slower-moving material ($300\text{--}400\text{ km s}^{-1}$) that originates from the region corresponding to the magnetic equator (Owens & Forsyth 2013). This slow solar wind belt is only about 20° in latitudinal width, but contributes enough to form the heliospheric current sheet, which is formed by the magnetic field boundary separating opposing magnetic field lines (Owens & Forsyth 2013). Interplanetary magnetic fields are highly variable on scales of 1 day to several solar rotations as the solar wind flows outward. That the *Voyager* spacecraft observed these fluctuations is no surprise, but some of the physical properties it measured were surprising. The magnetic field direction variability creates “sectors” of differing polarity which are based on extensions of magnetic fields from the polar regions of the Sun to the observing spacecraft.

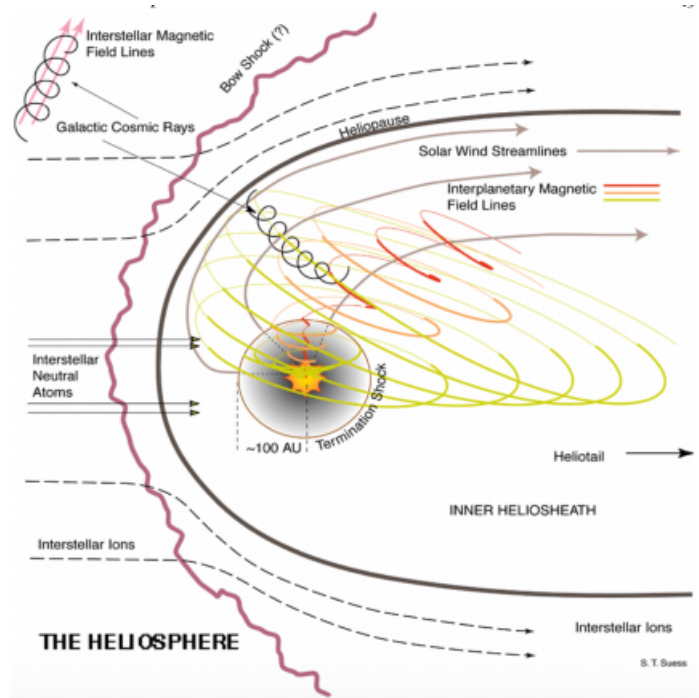


Figure 1.2: The complex structure of the heliosphere (from Stone et al. 2014).

Voyager 1 observed these sectors throughout its time in the heliospheric current sheet. Surprisingly, it remained in a positive sector for at least 125 days. Stone et al. (2005) postured that this sector was caused by reduced speeds behind an inward moving shock.

1.2.2 Heliospheric Termination Shock

The heliospheric termination shock (HTS) is the boundary where the solar wind decelerates from a cool supersonic flow to hot subsonic speeds (Burlaga et al. 2005; Stone et al. 2014). The solar wind pick-up ions are slowed, compressed, and therefore are heated. At the HTS, the solar wind decreases from 400 km s^{-1} to $\sim 130 \text{ km s}^{-1}$ in response to inward pressure from the local interstellar medium (Webber & McDonald 2013; Jokipii 2013). In 2004, *Voyager 1* crossed the HTS at a distance of 94 AU, while *Voyager 2* crossed at 84 AU in 2007 (Krimigis

et al. 2009). This inconsistency in the position of the HTS is due to asymmetry in the heliosphere, which varies with both time and location, as shown in Figure 1.3. *Voyager 2* measured the temperature and energy distribution of heliospheric plasma in the HTS, determining that the expansion of solar wind plasma heats up the HTS (Richardson et al. 2008). Both in situ and remote observations of the heliosphere and HTS have shown that the HTS is not perfectly spherical. The asymmetry is caused by a tilted interstellar magnetic field, which “blunts” the HTS at an angle relative to the orientation of the magnetic field (Jokipii 2013; Stone et al. 2014).

1.2.3 The Heliosheath, Heliopause, and Beyond

Beyond the termination shock lies the heliosheath, where the solar wind becomes subsonic. The heliosheath is both encompassed within the heliosphere and extended outward beyond the heliopause. The section located inside the heliopause is the inner heliosheath, and likewise, the section outside is the outer heliosheath (Schwadron et al. 2015). *Voyager 1* measured a large increase in interstellar plasma density after crossing the heliopause in 2012 (*Voyager 2* has not yet crossed this boundary, but is predicted to within the next five years).² The expected interstellar plasma density in the outer heliosheath is 0.1 cm^{-3} , and *Voyager 1* measured values of approximately 0.08 cm^{-3} , which is consistent with the expected value (Schwadron et al. 2015). Since the solar wind remains subsonic within the heliosheath, neutral interstellar ions can penetrate the heliosphere (Frisch et al. 2009).

The asymmetry of the HTS and heliosphere is also noted in Figure 1.3 as existing in the heliosheath. It explains a correlation between anomalous cosmic rays

²<http://voyager.jpl.nasa.gov/mission/interstellar.html>

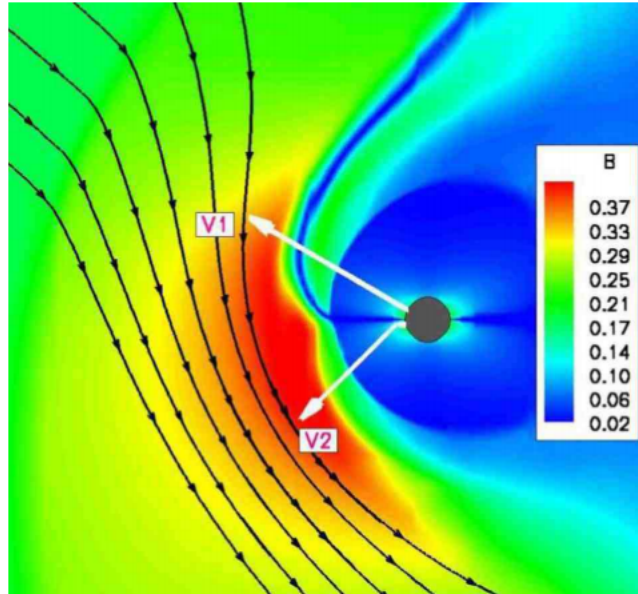


Figure 1.3: The contours of the interstellar magnetic field, with strength B (nT), are shown as black lines, while the white lines denote the trajectories of the *Voyager* spacecraft. The heliospheric current sheet within the heliosheath is deflected to the north (Opher et al. 2006).

(ACRs) and galactic cosmic rays (GCRs) observed (Frisch et al. 2009). ACRs are formed by the acceleration of pick-up ions, which are ionized interstellar neutral particles, while GCRs are charged particles, typically protons (Frisch et al. 2009; Blasi 2013).

At ~ 200 AU, there is a region known as the hydrogen wall (H-wall), which has a higher density of hydrogen atoms. As interstellar plasma flows through the solar system, it is slowed and heated by exchanges with solar wind protons (Linsky & Wood 1996). The H-wall results from coupling between the neutral components of the LISM and the magnetic fields and charged particles within the heliosphere. The signature of the H-wall is seen towards local stars in their Lyman- α absorption features (Linsky & Wood 1996).

In Figure 1.3, the interstellar magnetic field is parallel to the hydrogen deflection plane (HDP), which is defined by hydrogen and helium flow vectors. These

flow vectors differ from each other by only 4° , but their directions are similar enough to constrain the HDP to a plane inclined by 60° to the galactic plane (Opher et al. 2006). The HDP is also relatively close (within $\sim 2^\circ$) to the plane containing the Sun and undisturbed interstellar plasma flows (Grygorczuk et al. 2015).

Past the H-wall would typically be a bow shock, which is where the interstellar medium meets the solar wind, the density and pressure change rapidly, and the ISM flow slows to subsonic speeds (Sparavigna & Marazzato 2010). McComas et al. (2012) determined from measurements made by NASA’s *Interstellar Boundary Explorer* (hereafter, *IBEX*) that there is a bow “wave” of enhanced plasma density. *IBEX* measured an ISM velocity lower than the previous *Ulysses* results indicated (Witte 2004). Because this velocity is lower than the magnetosonic speed required to produce a shock, McComas et al. (2012) concluded that there is in fact no bow shock. This conclusion was supplemented by three different models created by Zank et al. (2013), who used magnetohydrodynamic plasma-kinetic hydrogen models with current LISM parameters. Their second model, which was constructed in three dimensions with an interstellar magnetic field strength of $3 \mu\text{G}$, yielded a ~ 200 AU thick shock-free structure.

Additional observations with *IBEX* revealed a new population of warm interstellar helium within the heliosphere. Kubiak et al. (2014) used detections of neutral interstellar helium to propose a new velocity-driven structure they call the “Warm Breeze.” The authors determined that the Warm Breeze is composed of a secondary population of neutral interstellar helium atoms, but were unable to definitively conclude on its origins. The most likely hypothesis is that the Warm Breeze is created due to charge exchange and scattering events between neutral and singly-ionized helium in the heliosheath (Kubiak et al. 2014). Alternatively,

the Warm Breeze could be simply a gust of neutral helium blown through the local interstellar cloud in a set of waves, which may be supported by its $\sim 19^\circ$ angle to the inflow of interstellar gas. This difference in inflow directions between hydrogen and helium was also observed as early as 1977 by Adams & Frisch (Frisch et al. 2009).

1.3 The Nature of the Interstellar Medium

As the Sun travels around the galactic center in its 220 million-year orbit, it passes through multiple clouds of gas, dust, and plasma. These clouds are the interstellar medium, or colloquially: the substance between stars. The interstellar medium contains the repository of building blocks necessary for star formation, and is replenished by stars at the end of their lifetimes as they deposit material either in the form of a supernova or a planetary nebula (McCray & Snow 1979). It therefore serves as a site for future star formation.

The local interstellar medium (LISM) forms the outer boundary for the heliosphere, and its behavior dictates the behavior of the Sun and heliosphere (Stone et al. 2014). The Solar System resides within the Local Bubble, which was formed by material blowing out of major star-formation regions in Scorpius and Centaurus (Mewaldt & Liewer 2000; Malamut et al. 2014). The Local Bubble is a region of low-density material extending for 50–200 pc within the local galactic neighborhood (Frisch et al. 2011). The Local Bubble includes the circum-heliospheric interstellar medium (CHISM), which sits at the edge of the Local Interstellar Cloud (LIC). The CHISM is the progenitor of interstellar gas and dust that flows through the heliosphere, and is relatively homogenous (Frisch et al. 2009). The LIC is one of a suite of warm, partially ionized clouds that make up the LISM.

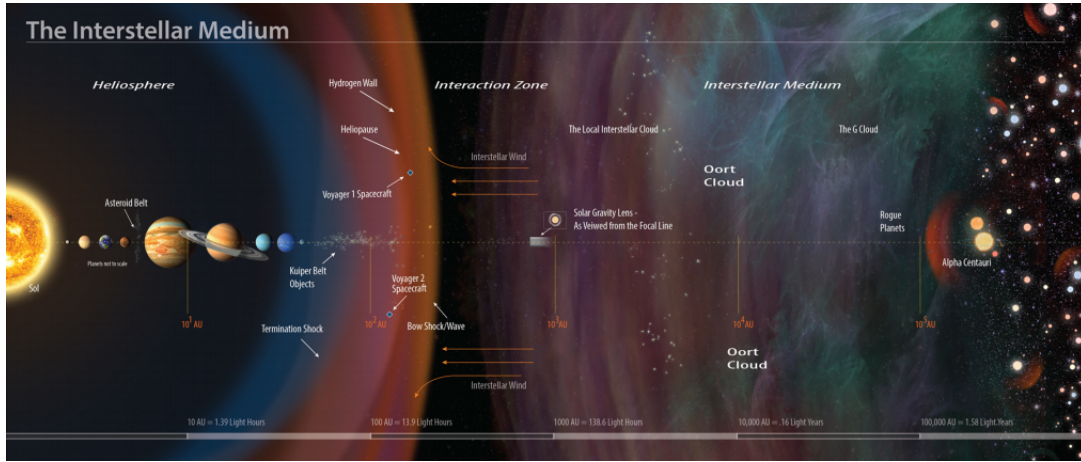


Figure 1.4: Artist’s rendering of the Solar System and local interstellar medium on a logarithmic scale (Stone et al. 2014).

At a certain point, “pristine” ISM interacts with “contaminants,” which contain atoms influenced by the heliosphere. McComas et al. (2015) determined that the location of the “pristine” ISM depends on the extent of the Sun’s gravitational influence and the position of the heliosphere relative to the interstellar gas upstream of it in the LISM. The Sun’s Hill Sphere, the region where its gravitational influence is strongest, extends out to nearly 5000 AU, not quite reaching the estimated inner edge of the Oort Cloud at 10,000 AU (Oort 1950; Morbidelli 2005; McComas et al. 2015). At this distance, the gravitational influence from the Galactic disk begins to take over, and particle interactions in the ISM are unaffected by the heliosphere. McComas et al. (2015) found that even at a distance of 1000 AU the ISM can be considered essentially pristine. At this point, gravitational bending (calculated from analytic solutions) is less than 0.1° and magnetohydrodynamic simulations show that there is no perturbation by the heliosphere on the LIC (Zank et al. 2013; McComas et al. 2015).

1.3.1 Interstellar Magnetic Fields

Mentioned briefly in conjunction with the shape of the heliosphere (see Sections 1.2.1 and 1.2.3), determining direction and magnitude of interstellar magnetic fields is key to understanding the interactions between the LISM and the heliosphere. The strength of interstellar magnetic fields (ISMF) affects the shape of the heliosphere and dictates the filtration of particles streaming into the Solar System (Opher et al. 2009). Until *Voyager 1* crossed the heliopause in 2012, no in situ measurements were available to directly measure the orientation of the ISMF. Early methods involved measuring polarization of light from nearby stars and measuring backscattered solar Lyman α radiation (Opher et al. 2009). Opher et al. (2006) suggested that a $\sim 2 \mu\text{G}$ ISMF in the HDP could account for observations of energetic shock particles by the *Voyager* spacecraft, with a field direction between $38\text{--}60^\circ$. However, the model used by Opher et al. (2006) neglected to include neutral hydrogen atoms, which led to underestimations of the strength of the ISMF in addition to large uncertainties in the field direction (Opher et al. 2009). Opher et al. (2009) followed up on the work by Opher et al. (2006) with new model constraints using *Voyager 2* observations of heliosheath flows. The orientation of the ISMF is determined by both the angle between the ISMF and the interstellar wind and the angle between the solar equator and the plane formed by the ISMF and interstellar wind (Opher et al. 2009). In order to account for the *Voyager* termination shock crossing distances, Opher et al. (2009) determined that the ISMF strength had to be between 3.7 and $5.5 \mu\text{G}$. Opher et al. (2009) also noted some discrepancies between their work and previous works with respect to ISMF orientation angle, and accounted for those differences as the result of ISM turbulence. ISM turbulence could cause the local magnetic field direction to differ

from that of the large-scale ISMF.

Burlaga & Ness (2016) used *Voyager 1* observations to constrain the local ISMF strength to 0.48 nT (or 4.8 μG), consistent with the range predicted by models from Opher et al. (2009). Additional modeling by Zirnstein et al. (2016) with *IBEX* data produced precise values for the magnitude and direction of pristine ISMF far (>1000 AU) from the Sun. Both sets of authors concluded that in situ measurements implied a draped strong ISMF around the heliosphere.

1.3.2 Gas Clouds

Much of the interstellar medium consists of low density, partially ionized gas coupled with dust. The ionization state of the gas depends on the local intensity of ultraviolet radiation needed to photodissociate or photoionize molecules (Draine 2009). Extreme-ultraviolet light from hot stars or white dwarfs provides sources of photoionization, causing an anisotropic gradient within the Local Bubble (Frisch et al. 2011). Inhomogeneous LISM clouds were only identified fifty years ago, and the first spectrum of interstellar gas outside the heliosphere was taken in 1977 with *Copernicus* (Adams & Frisch 1977; Frisch et al. 2009).

The majority of the LISM clouds consist of warm to hot neutral or ionized gas, though there are areas of cool gas. Photoionization provides a way to maintain the warm gas temperatures. Möbius et al. (2004) summarized previous interstellar helium parameters, including observations of the HeI 5870 Å line that provided measurements for gas temperature. A helium temperature of 6300 ± 340 K was derived from the measurements taken over the full duration of the *Ulysses* mission (Möbius et al. 2004), while temperatures between 5000 and 8000 K have been measured via long line-of-sight observations for 15 LISM clouds (Redfield & Linsky

2004b). These temperatures were found from measuring the absorption line widths of elements or ions with varying atomic weights in order to separate the thermal components from non-thermal ones (Linsky & Redfield 2014).

1.3.3 Dust Grains

In the 1990s, as it flew past Jupiter, *Ulysses* confirmed the presence of interstellar dust grains within the Solar System (Frisch et al. 2009). The dust, as expected, traveled with a speed and direction very similar to that of neutral interstellar hydrogen and helium gas. Dust particles have also been found by the in situ detectors on both *Galileo* and *Cassini* (Frisch et al. 2009). The properties of LISM dust have been inferred and measured by a wide range of techniques, including extinction and polarization of starlight, scattering, and thermal emission (Draine 2009). Since the interstellar clouds in the LISM were expected to be “diffuse clouds” largely consisting of neutral hydrogen and with low extinction coefficients, it was expected that the Local Bubble would be the same (Draine 2009). Spectroscopic features observed in the infrared showed silicate absorption, consistent with the assumption that most interstellar dust is composed of silicates or carbonates. *Ulysses* discovered that interstellar dust concentrations vary with solar cycle – that the dust concentration decreased during solar minimum due to solar wind filtering (Frisch et al. 2009). *Ulysses* also measured interstellar dust grain sizes, determining that grain size increased closer to the Sun. These observations, coupled with those from *Galileo* and *Cassini*, concluded that there is a dearth of small dust grains between 0.7 and 3 AU, implying that the interstellar dust stream is filtered by solar radiation pressure (Frisch et al. 2009).

Depletion occurs when heavy elements have gas phase abundances that are

less than the expected cosmic abundances, often because of varying levels of incorporation into interstellar dust grains. In mathematical terms, depletion can be defined as either linear or logarithmic, reflecting the linear and logarithmic gas phase abundances referenced to cosmic or solar abundances (Savage & Sembach 1996). However, one caveat is that depletions do not always take into account partial ionization of hydrogen (Redfield & Linsky 2008). In the LISM, elemental depletion gives rise to the need for ionization corrections. The number of atoms that must be depleted onto dust grains can also be calculated based on pickup ion isotope ratios (Frisch et al. 2011). Additionally, depletion onto dust grains in the ISM clouds depends on the condensation temperature of the element in question. Therefore, elements with the highest condensation temperatures are the most depleted in the ISM, and the gas phase abundances of volatile elements are higher in warm clouds (Frisch et al. 2011; Savage & Sembach 1996). Small depletions are well-correlated with high turbulent velocities, suggesting that the destruction of dust grains may have returned specific ions to their gas phase. It is entirely possible that dust destruction was caused by shocks produced by supernovae or by turbulent motions driven by interaction between clouds or even by direct collisions (Redfield & Linsky 2008).

1.3.4 Kinematic Structure

The kinematic structure of the LISM is fairly complicated, with multiple absorbers along many sight lines. Early analysis of titanium absorption line spectra for stars within 100 pc by Crutcher (1982) found that warm gas within the LISM moves with a coherent heliospheric velocity. Crutcher (1982) determined that the direction of the gas was consistent with that of an expanding shell of gas acceler-

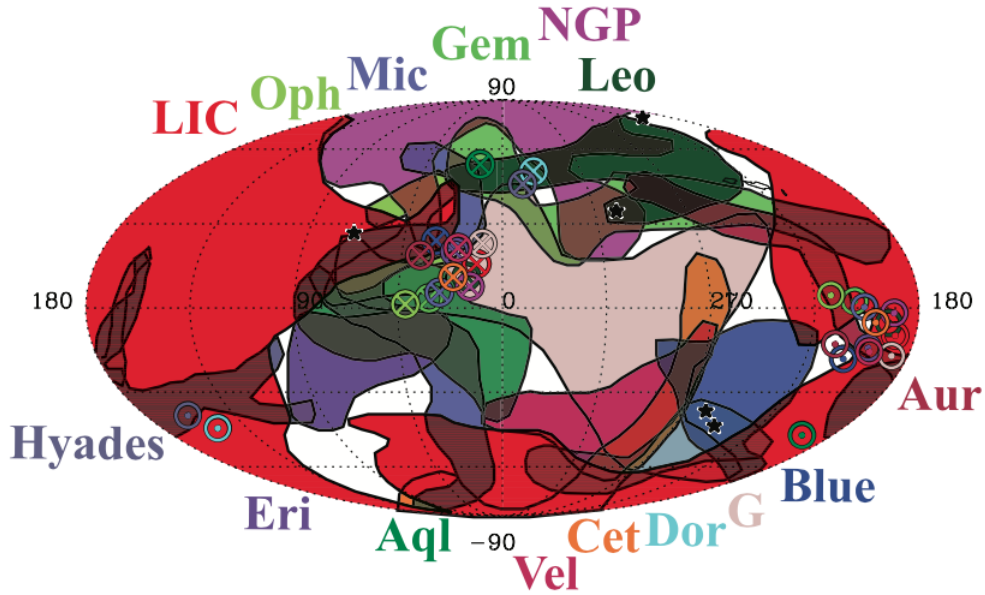


Figure 1.5: The dynamical cloud morphologies determined by Redfield & Linsky (2008) are overlaid in galactic coordinates and color-coded, with the upwind heliocentric velocity vector direction indicated by the circled cross and the downwind vector direction given by the circled dot. The black outlines indicate sharp edges of the clouds. The black stars represent sources of radio scintillation as studied by (Linsky et al. 2008).

ated by both hot stars and supernovae from the Scorpius-Centaurus Association – the nearest OB association to the Sun (Redfield & Linsky 2015).

Frisch et al. (2002) and Redfield & Linsky (2004a) developed the basis for the current best kinematic model of the LISM, which was created by Redfield & Linsky (2008). Redfield & Linsky (2008) based their kinematic model off of a large data set containing 270 individual velocity components along 157 different lines of sight through the LISM. They also used high-resolution *Hubble Space Telescope* spectra from the Goddard High Resolution Spectrograph and the Space Telescope Imaging Spectrograph for 55 velocity components to measure absorption line width from ions of different atomic weight in order to determine the temperature and turbulent velocity (Redfield & Linsky 2004b). The model by Redfield & Linsky (2008) includes 15 distinct clouds. These component clouds

are individual co-moving structures of partially ionized gas identified by common velocities across large patches of the sky (Redfield & Linsky 2015). In order to determine the morphology of these clouds, Redfield & Linsky (2008) assumed that the interstellar gas flow inside each cloud is coherent and that the clouds have sharp edges. The names of these clouds are either historical or based off of their locations in the sky relative to named constellations (Redfield & Linsky 2008).

1.4 *Hubble Space Telescope*

The *Hubble Space Telescope* (*HST*) was launched from Cape Canaveral, FL on April 24, 1990 aboard the Space Shuttle *Discovery*. The culmination of ten years and \$1.6 billion, *HST* was designed to be the newest and most advanced space telescope of its generation and the next (Goodwin & Cioffi 1994). While launch was originally scheduled for early 1986, the *Challenger* disaster forced NASA to delay *HST*'s launch and deployment for another four years (Shayler & Harland 2016). A day after its launch, on April 25, 1990, *HST* was deployed into a low-Earth orbit at an altitude of approximately 570 km (Xapsos et al. 2014). The initial main objective of the space telescope initiative proposed by NASA (as early as the early 1970s) was to launch a 2.4 m telescope “with excellent optical quality into orbit to obtain unmatched spatial resolution and ultraviolet sensitivity” (Robberto et al. 2000). *HST* was the first of NASA’s “Great Observatories” to be launched, and it was swiftly followed by the *Compton Gamma Ray Observatory* in 1991, *Chandra X-Ray Observatory* in 1999, and the *Spitzer Space Telescope* in 2003 (Shayler & Harland 2016).

³<http://hubblesite.org/image/3831/spacecraft>



Figure 1.6: *HST* as seen from the *Space Shuttle Discovery* during its second servicing mission in February 1997.³

HST is composed of three main elements that control its movement, protect it from the hazards of space, and dictate its observations. These elements are the Support System Module, the Optical Telescope Assembly, and the Scientific Experiment Package (Shayler & Harland 2016). The Support System Module houses all the servicing systems aboard the telescope in addition both controlling communications to the ground and directing *HST*'s scientific instruments. These communications are controlled by the Data Management System, which also receives data from the various systems in the Optical Telescope Assembly (Shayler & Harland 2016). *HST* hosts a highly precise pointing system that enables the telescope to point within 0.01 arcseconds of its target and remain relatively stable over the course of 24 hours. The telescope is powered by two solar panel arrays and six NiH₂ batteries, which are used when the demands of the telescope exceed the power provided by the solar panels (Shayler & Harland 2016). The Optical Telescope Assembly houses the 2.4 m primary mirror and support instrumentation.

The Scientific Equipment package includes all scientific instruments, which have varied over the course of the telescope's lifetime. Currently, there are five main scientific instruments still operational on *HST*. These instruments are the Space Telescope Imaging Spectrograph (STIS), the Wide Field Camera 3 (WFC3), the Advanced Camera for Surveys (ACS), the Fine Guidance Sensors (FGS), and the Cosmic Origins Spectrograph (COS).

1.5 Connections to *Voyager*

This work is able to take advantage of the advanced capabilities of the Space Telescope Imaging Spectrograph (see Section 2.1) and use high-resolution spectra of four nearby stars along the sight lines of the *Voyager* spacecraft to compare with in situ data from the spacecraft themselves. The spectra provide a host of quantitative measurements of nearby ISM gas, including fundamental physical properties such as kinematic structure, electron density, and temperature and turbulence. By observing stars within 15° of the lines of sight of the *Voyagers*, we are able to create a direct connection to the in situ measurements taken by the spacecraft. Though the *HST* spectra provide a far larger overview, we can predict what kind of ISM environment the *Voyagers* may one day travel through.

Chapter 2

Observations and Data Reduction

2.1 Space Telescope Imaging Spectrograph

In 1997, the Space Shuttle *Discovery* replaced *HST*'s Goddard High Resolution Spectrograph and Faint Object Spectrograph with a new second-generation spectrograph, the Space Telescope Imaging Spectrograph (STIS). Unlike the previous first-generation, one-dimensional spectrographs, STIS could be used as a general-purpose spectrograph, observing across a wide range (1150–10000 Å) of wavelengths and a large number of very different astrophysical targets. The principle reasons why STIS was, and still is, such a crucial instrument stem from its use of large format, two-dimensional array detectors (Kimble et al. 1998). There are three detectors: two Cs₂Te Multi-anode Microchannel Array (MAMA) detectors for measurements in the ultraviolet, and one Charge-Coupled Device covering the visible spectrum (Kimble et al. 1998). The STIS spectrographs use sixteen different diffraction gratings, twelve of which are used in the first order and four of which are echelle gratings used for higher diffraction orders (Woodgate et al. 1998). Unlike typical diffraction gratings, echelle gratings have relatively low groove densities, but have groove shapes optimized for use at high diffraction angles (i.e. grazing angles).

2.2 Observations

The data for this project were obtained on *HST*/STIS over four non-consecutive times between August and October 2015. Each individual observation was devoted to one target star, with observations taken over the course of 4–8 hours. A full table of observation parameters is given in Table 2.1.

All of the data for this work were taken either in the near-UV or far-UV wavelength range between 1150–3100 Å using the MAMA detectors (NUV-MAMA and FUV-MAMA) (Kimble et al. 1998). The high spectral resolution capabilities of STIS were needed to model the ISM absorption line profiles because they are intrinsically narrow, and to resolve the velocity components of ISM clouds because they are often closely-spaced in radial velocity. With both absorption line profiles and resolved velocity components, we can take accurate physical measurements of the temperature, turbulent velocity, and ionization. Additionally, a high signal-to-noise ratio (S/N) was needed to detect weak absorption lines. The MAMA detectors use high-conductance single, curved micro-channel plate intensifiers, capable of 200 counts per second per pixel, with electronics that run at 300,000 counts per second, and are thus able to obtain a large number of continuum counts per resolution element (Woodgate et al. 1998). Both detectors are capable of providing high-resolution spectra with array sizes of 2048×2048 pixels and spectral resolutions of less than $30 \mu\text{m}$ (Woodgate et al. 1998).

The observations utilized three of the four higher-order echelle gratings, which are E230H, E140M, and E140H. These gratings have resolving powers of 92,300 to 110,900, 46,000, and 99,300 to 114,000, respectively (Kimble et al. 1998). Resolution is calculated as $R = \frac{\lambda}{\Delta\lambda}$, or is defined by the full-width at half-maximum of an unresolved spectral line. The E230H grating was used with the NUV-MAMA

detector for three total orbits and provided spectra over a wavelength range of 2576–2812 Å. This grating was chosen in order to observe the MgII (2796, 2803Å) and FeII (2586, 2600Å) ions, which are not significantly thermally broadened, but provide sharp line profiles to resolve line-of-sight velocity structure. For all four target stars, the central wavelength of the E230H observations was 2713 Å. The E140M grating was used to observe the Lyman- α line of HI (1215 Å), which has a broad absorption profile. This setting was used with the FUV-MAMA detector, providing a wavelength range of 1144–1710 Å, with a central wavelength of 1425 Å. The E140H grating has several different settings, each extending over small, separate ranges of wavelengths. We used a setting that extended over wavelengths between 1176–1372 Å, with a central wavelength of 1271 Å. The echelle lengths for all grating settings were 0.2 arcseconds, though the widths differed depending on the aperture. The E140M grating utilized the 0.2×0.2 aperture, which has a width of 0.2 arcseconds, while the E230H and E140H gratings used the 0.2×0.09 aperture, with a width of 0.09 arcseconds (Woodgate et al. 1998).

2.3 Data Reduction

The MAMA detectors produce a two-dimensional UV image, where the number of data numbers per pixel is limited to the total number of photons per pixel that can be accumulated in a single exposure (Bostroem & Proffitt 2011). The Space Telescope Science Institute (STScI) developed a data reduction pipeline, `calstis`, that: performs basic, 2D image reduction to produce a flat-fielded output image; performs 2D and 1D spectral extraction to produce either a flux-calibrated spectroscopic image or a 1D spectrum of flux versus wavelength (Bostroem & Proffitt 2011). The data are then presented in the form of flexible image transport (FITS) files. The `calstis` pipeline also propagates statistical errors and tracks the quality of the data throughout the calibration, flagging when bad pixels are present. For wavelength calibration, onboard Pt-Cr/Ne calibration lamps are used, followed up by `calstis` processing the associated wave-calibrated exposure to determine the zero point offset of the wavelength and spatial scales in the science image (Bostroem & Proffitt 2011; Bristow et al. 2006).

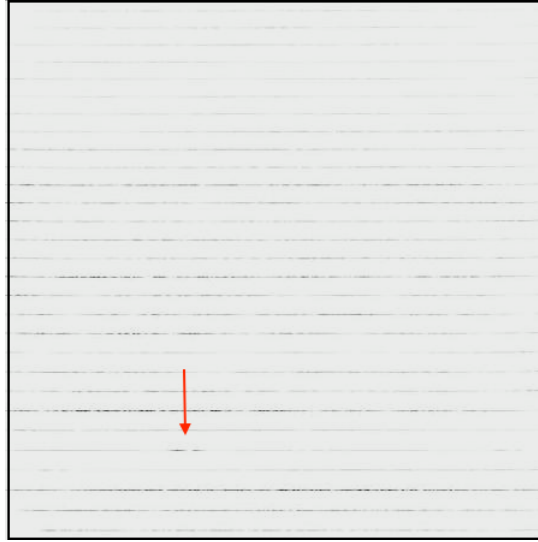


Figure 2.1: Raw STIS spectra for GJ 780, the brightest of the four target stars. The horizontal white lines represent echelle orders, where wavelength increases left to right within the order and top to bottom between orders. The red arrow denotes the MgII 2796Å line. The LISM absorption can be seen in the middle of the MgII emission line.

2.4 Target Stars

The target stars for observations with *HST*/STIS were selected for their angular separations from the *Voyager* lines of sight. Until these observations were taken in 2015, there were no observations of any nearby (<100 pc) stars within 15° of the *Voyager* spacecraft. All but one of the target stars are M-dwarfs, with sizes ranging between $0.18\text{--}0.991M_\odot$ and $0.214\text{--}1.223R_\odot$. The fourth star, GJ 780, is a late G-type star similar in size to the Sun, and therefore much brighter and larger than the others. The use of two targets per sight line allows for derivation of small-scale structure in the material just outside the heliosphere since the nearest sight lines provide relatively simple interstellar absorption profiles (Malamut et al. 2014). Additionally, two targets per sight line provided some redundancy in case we did not detect any LISM absorption in one of the spectra. The stellar parameters and angles from the *Voyager* sight lines are presented in Table 2.2.

Table 2.2: Stellar parameters for the target stars along the lines of sight toward the *Voyager* spacecraft. Galactic coordinates from the SIMBAD Astronomical Database.

| Gliese # | Other Name | Spectral Type | l (deg) | b (deg) | Mass (M_{\odot}) | Radius (R_{\odot}) | T_{eff} (K) | V_{radial} (km s^{-1}) | m_V (mag) | $\Delta\theta$ (deg) | Distance (pc) |
|------------------|--------------|---------------------|-----------|-----------|----------------------|------------------------|-------------------|-------------------------------------|--------------------|----------------------|---|
| <i>Voyager 1</i> | | | | | | | | | | | |
| GJ 678.1A | HIP 85665 | M1.0Ve ^a | 028.5748 | +20.5423 | 0.549 ^b | 0.543 ^b | 3675 ^b | -12.51 ^c | 9.433 ^d | 8.1 | 9.98 ± 0.11 ^e |
| GJ 686 | HIP 86287 | M1.5Ve ^a | 042.2402 | +24.2968 | 0.445 | 0.418 | 3657 ^b | -9.55 ^c | 9.577 | 9.0 | 8.09 ± 0.11 ^e |
| <i>Voyager 2</i> | | | | | | | | | | | |
| GJ 780 | δ Pav | G8IV ^f | 329.7673 | -32.4165 | 0.991 ^g | 1.223 ^h | 5652 ⁱ | -21.7 ^j | 4.62 ^h | 9.2 | 6.11 ± 0.03 ^k |
| GJ 754 | LHS 60 | M4V ^l | 352.3601 | -23.9018 | 0.180 ^l | 0.214 | 2950 ^m | 16.0 ⁿ | 12.23 ^o | 13.1 | 5.71 ^{+0.27p} _{-0.25} |

^aLépine et al. (2013)^bMann et al. (2015)^cNidever et al. (2002)^dZacharias et al. (2012)^eKoen et al. (2010)^fGray et al. (2006)^gTakeda et al. (2007)^hSousa et al. (2008)ⁱMaldonado et al. (2015)^jEvans (1967)^kvan Leeuwen (2007)^lBonfils et al. (2013)^mPhillips et al. (2010)ⁿRodgers & Eggen (1974)^oMermilliod (1986)^pGliese (1969)

Chapter 3

Fitting and Results

3.1 Interstellar Ions

One of the most common ways to study the LISM is to observe absorption features against nearby background sources (Malamut et al. 2014). The most important resonance lines of ISM ions are found at UV wavelengths, which is why observing with *HST*/STIS is extremely useful. The ISM has a relatively low gas density, which means that the gas atoms and electrons are in a low excitation state. As such, we can assume that all atoms are in the ground state. In order to view absorption of background photons, the atoms must be excited from the ground state into resonance lines (Dyson & Williams 2003).

Through ground-based observations, species including the atoms LiI, NaI, CaI, CaII, KI, FeI, and TiII and the molecules CH, CH⁺, CN, C₂, and NH can be detected along long sight lines. We have short sight lines, and therefore using a space-based telescope is our only option for detecting UV absorption by abundant atoms like C, N, O, Mg, Si, and Fe in a number of different ionization states (Savage & Sembach 1996). *HST*/STIS has successfully detected elements and ions observed in nearby ISM clouds, including HI, DI, CI, CII, CIV, NI, OI, AIII, SiII, SiIII, SiIV, MgI, MgII, SII, and Fe II (Frisch et al. 2011).

Multiple ISM component absorption features can be fully resolved with high

spectral resolution observations, allowing for identification and characterization of the associated clouds. Short sight lines, like those utilized in this work, permit detailed study of warm LISM material, since absorptions are less likely to be as blended or saturated compared to long ($\sim 100\text{--}1000$ pc) sight lines (Malamut et al. 2014). Resonance lines of heavy ions are best able to measure the velocity structure along a particular line of sight. High-resolution spectra of heavy ions and lower-resolution spectra of lighter ions can be coupled together in order to determine several fundamental properties of the LISM, including morphology, small-scale structure, temperature, and turbulence (Redfield & Linsky 2004a). Singly-ionized magnesium (MgII) and iron (FeII) are among the most important heavier elements observed in the LISM, since they have high cosmic abundances. Heavy ions can also provide information about the kinematic structure of LISM component absorbers because they are less impacted by thermal broadening and blending. By using heavy ions, we can easily identify multiple ISM components along a particular line of sight (Malamut et al. 2014). Blending often results from the presence of additional lines or with a rising stellar continuum, as is often the case with FeII (Redfield & Linsky 2004a).

Presented in Table 3.1 is an overview of all detected ISM ions in the data used in this work. The table contains the rest wavelengths of the ions, as well as the associated gamma values and oscillator strengths. The gamma value is the natural damping constant, γ , which is the sum of all the Einstein coefficients to lower energy levels (Morton 2003). The oscillator strength (or f -value) is defined as the probability of absorption of electromagnetic radiation in transitions between energy levels. In general, for high oscillator strengths, we see deeper absorption in the line profile.

Table 3.1: Detected interstellar ions in the near and far UV for the data used in this work. All parameters from Morton (1991, 2003).

| Ion | Wavelength (Å) | Gamma (10^8 s^{-1}) | Oscillator Strength |
|------|-------------------|------------------------------------|------------------------|
| HI | 1215.6682 | 6.265 | 0.2776 |
| | 1215.6700 | 6.265 | 0.4164 |
| | 1215.6736 | 6.265 | 0.1388 |
| DI | 1215.3376 | 6.270 | 0.2777 |
| | 1215.3394 | 6.270 | 0.4165 |
| | 1215.3430 | 6.270 | 0.1388 |
| CII | 1334.5323 | 2.880 | 0.1278 |
| CII* | 1335.6627 | 2.880 | 0.0128 |
| | 1335.7077 | 2.880 | 0.1280 |
| OI | 1302.1685 | 5.650 | 4.80×10^{-2} |
| MgII | 2796.3543 | 2.625 | 0.6155 |
| | 2803.5315 | 2.595 | 0.3058 |

There are, of course, many more interstellar ions than are listed in this work, as only a small fraction were detected in the data. Table 3.1 is representative of detected emission lines also containing interstellar absorption from the star GJ 780, which is the brightest of the four target stars.

3.2 The Fitting Procedure

3.2.1 Continuum

The first step in the fitting process is to fit stellar continua to each spectrum. Each continuum includes the blackbody radiation intrinsic to the star combined with any stellar emission or absorption features. For hot stars, we see mainly continuum emission, but for cool stars like those used in this project, we see stellar line emission (see Figure 3.1). The IDL routine `mkfb`, written by S. Redfield, predicts the stellar continuum as it would appear without any ISM absorption.

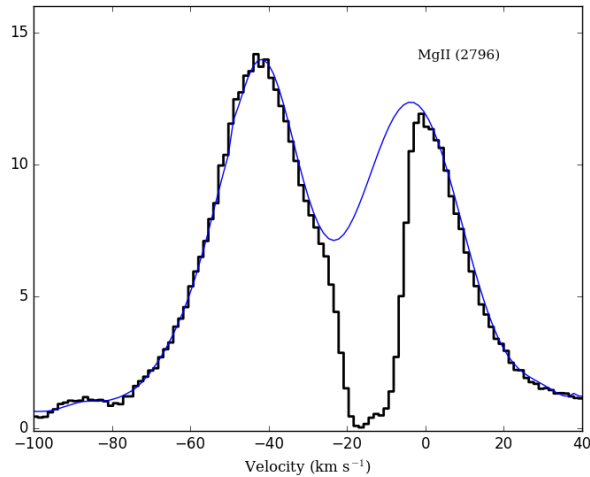


Figure 3.1: Presented above is the reconstructed stellar continuum (indicated by the blue line) for the MgII 2796 Å line in GJ 780. The black histogram is the observed flux data. This continuum was estimated by fitting a polynomial of order 8 to the areas just red-ward and blue-ward of the absorption. We know that MgII often has a characteristic double-peaked shape due to a temperature inversion in the stellar chromosphere (Kohl & Parkinson 1976).

In order to run `mkfb`, it is necessary to identify the absorption features due to interstellar clouds along the line of sight. The continuum placement requires an estimate of emission line flux at the absorbing line wavelength (Redfield & Linsky 2002). Typically, the continuum can be fit with a simple, low order polynomial. The program uses a least-square polynomial fit of order 1 to 10 to the regions both just red-ward and blue-ward of the absorption feature. In the case when the interstellar absorption is far from the line center, the unobserved stellar flux can be estimated by flipping the emission line about the stellar rest frame (Redfield & Linsky 2002). It is crucial to get the best possible estimate for the intrinsic stellar continuum upon which the interstellar absorption is superimposed, since uncertainties in this assumed profile can cause larger errors later on in the fitting process (Linsky & Wood 1996).

3.2.2 ISM Absorption

Once we create the intrinsic, unobserved stellar continuum, we can begin the next step in the fitting process. Initially, each fit begins with one absorption component, unless it is evident from visual inspection of the data that there are multiple absorbing clouds. We analyze each line profile without imposing any constraints on the characterizing parameters beyond trying to minimize the χ^2 value. The IDL routine `gismfit`, written by S. Redfield and B. Wood, utilizes a Marquardt least-squares algorithm to fit Gaussian absorption profiles to the data. `gismfit` queries initial guesses for Doppler parameter, absorption centroid wavelength, and log column density, and requires the background continuum from `mkfb`, varying all parameters until a minimum χ^2 is found. The Doppler parameter (b value) defines the width of the absorption feature, and varies from ion to ion. If a physically possible b value cannot be obtained by a fit, then we can freeze this parameter at the average value for the particular ion. The absorption centroid wavelength is an estimate of the center of the absorption feature. We can sometimes use a given velocity (i.e. one from the LISM Dynamic Model Kinematic Calculator) and calculate the expected central wavelength by using a simple Doppler shift calculation. The column density is the number of ions or atoms per unit area integrated along a particular path. In `gismfit` input, column density is expressed in logarithmic form, and typical values for ions other than HI are between $10^{12} - 10^{15} \text{ cm}^{-2}$. We take rest wavelengths and oscillator strengths from Morton (1991, 2003), which are given in Table 3.1. The input file for `gismfit` also includes the instrumental line spread function (LSF) for STIS, provided by Bostroem & Proffitt (2011). The LSF is the instrumental profile, which is a convolution of the response functions of both the mirror and the spectrograph grating.

Sometimes, if the initial guesses are not well-constrained, the program will create a fit that is not physically accurate. In that case, the guesses will need to be altered and the program must be rerun until a more acceptable fit is reached.

We typically start with one absorption component in the initial fit, but many absorption features may contain more than one component. In order to determine the number of absorbers, we start from one component and increase the number of absorbers as warranted by the data until the quality of the fit improves (Redfield & Linsky 2002). With the addition of each component, the χ^2 value decreases. At a certain point, continuing to increase the number of components no longer significantly improves the quality of the fit, and we use an F-test to determine if additional components are statistically justified. An F-test compares two reduced χ^2 values with one value designated as “better” (lower χ^2) and the other as “worse” (higher χ^2). We take the ratio of the worse χ^2 to the better one, and compare the result (F) to a calculated distribution. The IDL function `f_cvf` calculates the cutoff value “V” in a distribution “F” with the number degrees of freedom from both of the reduce χ^2 values. If the calculated F is less than the result of the first ratio, then the fit is significantly better. Conversely, if the calculated F is greater, then the two variances are equal and the “better” fit is not statistically justified.

Certain ions – singly-ionized iron, magnesium, and manganese – contain multiple resonance lines per single wavelength range. Each line contains the same components at the same radial velocity, with the same number of identical line widths and column densities, and therefore can be fit simultaneously (Redfield & Linsky 2002). The two lines of a doublet provide independent measurements of the same ion. The difference in oscillator strengths between the components of the doublet allows for accurate constraints on interstellar absorption parameters, the stellar continuum flux, and number of absorbing components. Simultaneous

fits provide a better determination of interstellar absorption parameters than that from an individual fit, though we also perform individual fits for comparison. Systematic errors, such as continuum placement, may dominate the statistical errors (Redfield & Linsky 2002). We were able to simultaneously fit to the MgII doublet in both GJ 780 and HIP 85665. The fits are presented in Figures 3.3 and 3.5.

3.2.3 Error Analysis

Once the initial best-fit models are produced by `gismfit`, Monte Carlo error analysis can be run to determine the uncertainty on each parameter. The Monte Carlo method relies on generating random inputs and determining which fraction of those inputs obeys the properties generated by the model from `gismfit`. As the number of random inputs, or trials, increases, the probability of the outcome increases, and so the approximation improves (Metropolis & Ulam 1949). In Tables 3.2–3.4, we present, for single ion fits (i.e. OI, CII, etc.), the final parameter values and uncertainties as generated by Monte Carlo error analysis unless otherwise noted. For the ions containing multiple resonance lines within the same wavelength range (i.e. MgII, FeII, etc.), we perform three fits; one for each line of the doublet, and a final simultaneous fit to both. The parameter values for these ions are the weighted mean of the three values generated by the three fits we create. The associated uncertainties are either the weighted mean errors or the standard deviation, whichever is the largest numerical value. Ideally, the three fits should yield similar parameter values, but often, systematic errors occur. Typically, it is straightforward to place the continuum, especially given that we have high-resolution spectra. However, sometimes, if a line is particularly broad, it can be difficult to accurately place the continuum. The uncertainty in

continuum placement can give rise to systematic errors. Blending occurs when there is significant overlap between ISM components in a particular line. This is usually prevalent in long sight line observations, but is common to the UV. There are numerous important atomic transitions that occur in the UV, and often, they are overlooked if spectra do not have high enough resolution (Frisch et al. 2011). Thermal broadening is caused thermal or large-scale turbulent motion of individual atoms or ions in a gas. It is dependent on the mass of the ion, the frequency of the observed spectral line, and the temperature of the gas. Thermal broadening dominates for the lightest ions like HI and DI, and is almost certainly a cause of the broad absorption profiles we see in both lines (Redfield & Linsky 2004a).

3.3 Fits

We were able to fit interstellar absorption in three of the four sight lines. Though every sight line contains the Lyman α line of HI at 1215 Å, the ISM analysis of the Ly α line has not yet been completed due to the complexity of the line, which not only includes ISM absorption, but also geocoronal emission, and heliospheric or astrospheric absorption signatures. In addition to broad absorption, ISM HI column densities are high enough that the absorption profile also has wide, extended damping wings (Wood et al. 2005). In order to perform an analysis of the Ly α line of HI, we must first reconstruct the entire stellar profile. For further discussion of the HI Lyman α line, see Section 3.6.

Presented in Figure 3.2 is the MgII data from GJ 754 and HIP 86287. Both stars are M stars, meaning they likely have variable activity levels in addition to being relatively faint. Because of the low S/N, we were unable to detect and fit the MgII ISM absorption along the sight lines. Typically, we would start by

fitting ISM absorption in the MgII doublet to get a baseline for velocity component values. However, since we do not definitively detect any ISM absorption, we were unable to do this. We do show velocities of known ISM clouds predicted to lie along the line of sight to these two stars. We note that there is a large shift in the radial velocity of the star in comparison with the predicted velocities of the ISM clouds. We also see that the ISM cloud velocities predicted by Redfield & Linsky (2008) do not appear to coincide with any significant absorption.

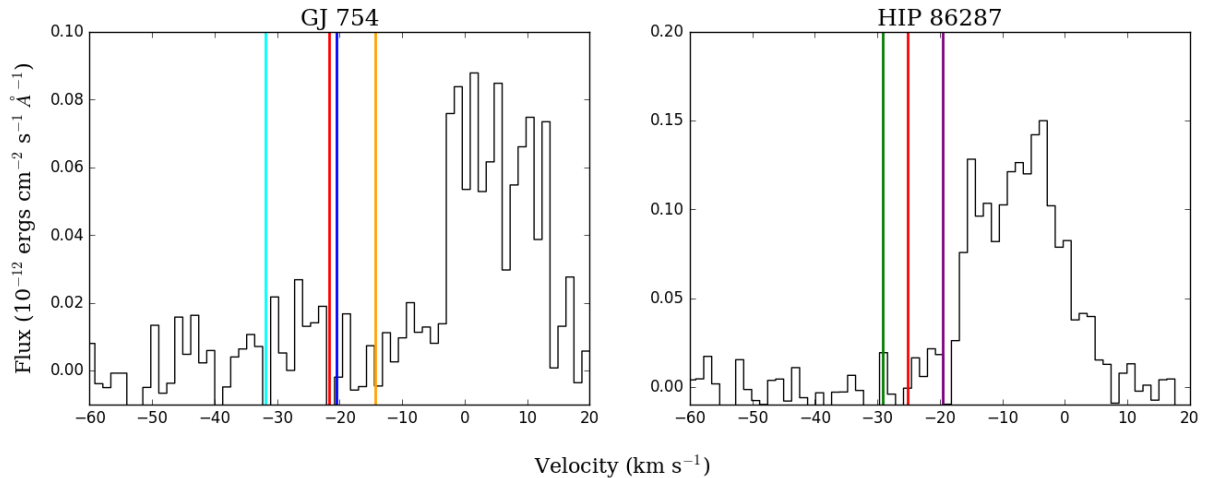


Figure 3.2: Presented above is the MgII 2796Å line for both GJ 754 and HIP 85665. The black histogram is the observed flux data plotted in velocity space. The colored vertical lines indicate velocities of the LISM clouds predicted to lie within 10° of the star (Redfield & Linsky 2008). The red line is the Mic cloud, blue is the G cloud, cyan is the Vel cloud, orange is the Aql cloud, green is the Oph cloud, and purple is the LIC.

We now present our fits to three of four sight lines. For GJ 780, we were able to simultaneously fit both CII and CII* and the MgII doublet. We performed an individual fit to the OI 1302 Å line and to the DI line of Ly α . Additionally, we see both lines of the MgII doublet and DI in HIP 85665. We were also successful in fitting to DI in GJ 754. The fits to these stars are presented in Figures 3.3–3.5.

We can clearly see significant ISM absorption in GJ 780 in all observed ions. We note that both CII and OI are saturated. The small bump in the absorption

in MgII 2803 Å at around -10 km s^{-1} is due to the presence of a second ISM component. Therefore, from the MgII doublet, we were able to determine that there were two absorption components present in the data. The third component in OI is due to geocoronal absorption, and will be explored in greater detail in Section 3.4.2. We performed a simultaneous fit to CII and CII* as a proxy for measuring electron density.

Though it may appear that there are multiple absorption components in the Ly α line of DI in GJ 754, we determined that there were only two. Two features seen at -10 km s^{-1} and at -35 km s^{-1} at first glance seemed to be absorption features, but upon further investigation of the fit parameters, we found that they were far too narrow to be deuterium absorption features. Typically, DI absorption features have large Doppler parameters, which is indicative of broad absorption features. We also note that the signal-to-noise ratio of this particular spectrum is well below 10. A likely cause for the low S/N is that GJ 754 is a twelfth-magnitude star and is much fainter than any of the other targets.

In HIP 85665, we also determined that there were only two absorption components. While the slight dip in flux at -10 km s^{-1} could be fit with a third component, it is simply a stellar radial velocity feature. We detected MgII absorption in both lines and successfully performed a simultaneous fit.

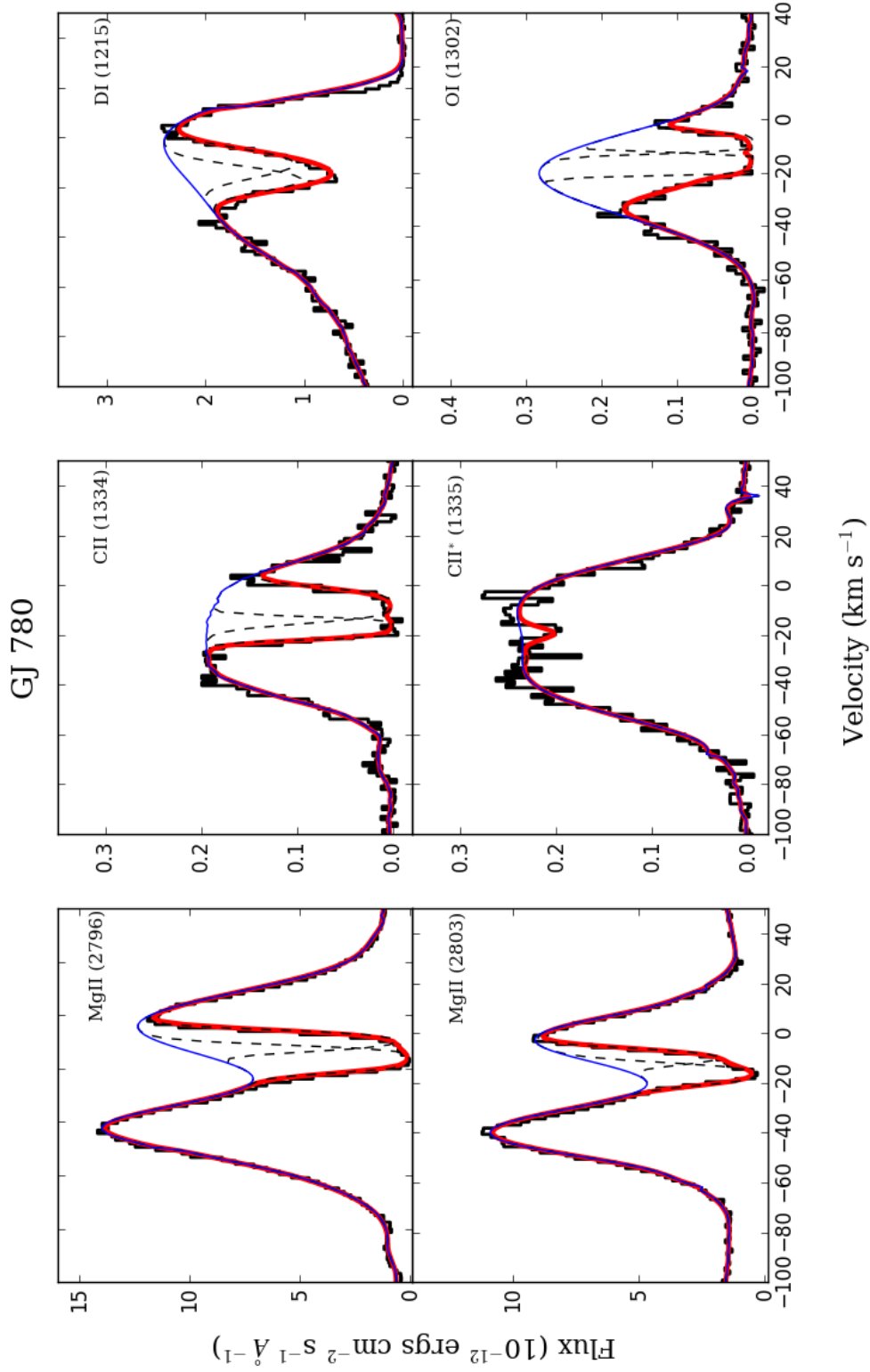


Figure 3.3: Best-fit results from the fitting procedure. The black histogram is the observed flux data. The blue solid line is the estimated stellar continuum, which includes the intrinsic chromospheric emission lines of the star. The dashed black lines are the profiles of each absorption component, and the red line is the convolution of the assumed intrinsic stellar emission line folded through the interstellar absorption.

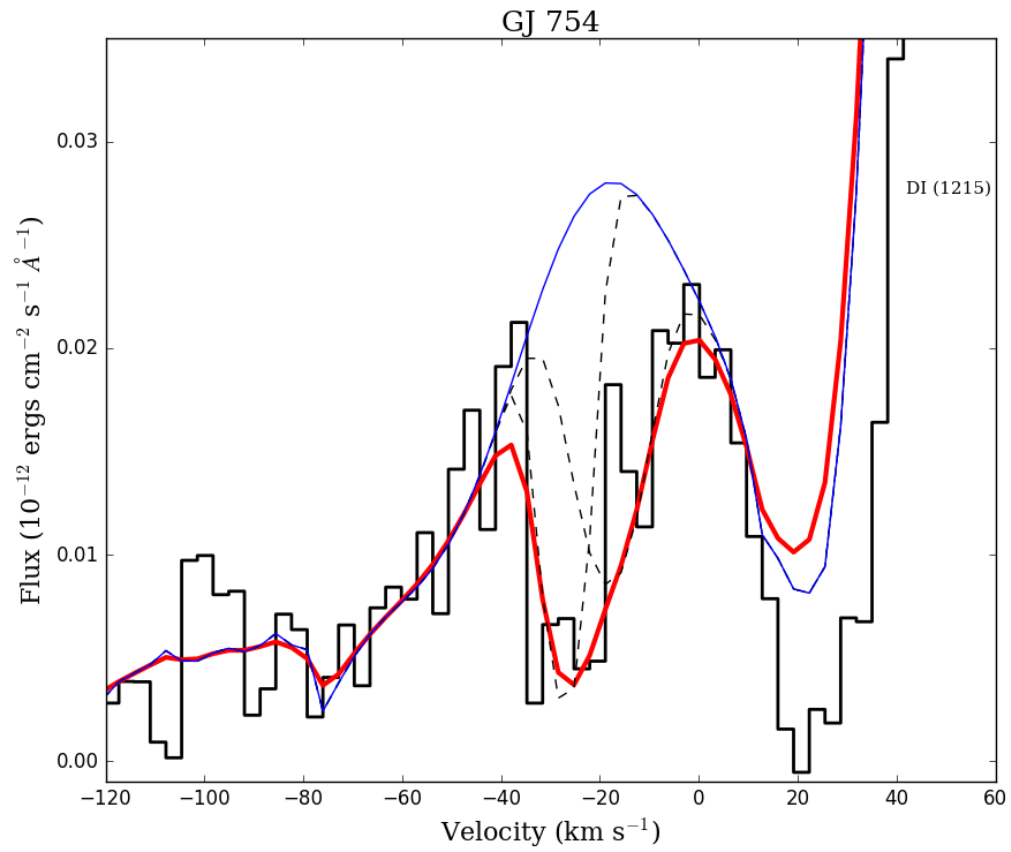


Figure 3.4: Same as Figure 3.3, but for the GJ 754 sight line, where only DI showed ISM absorption.

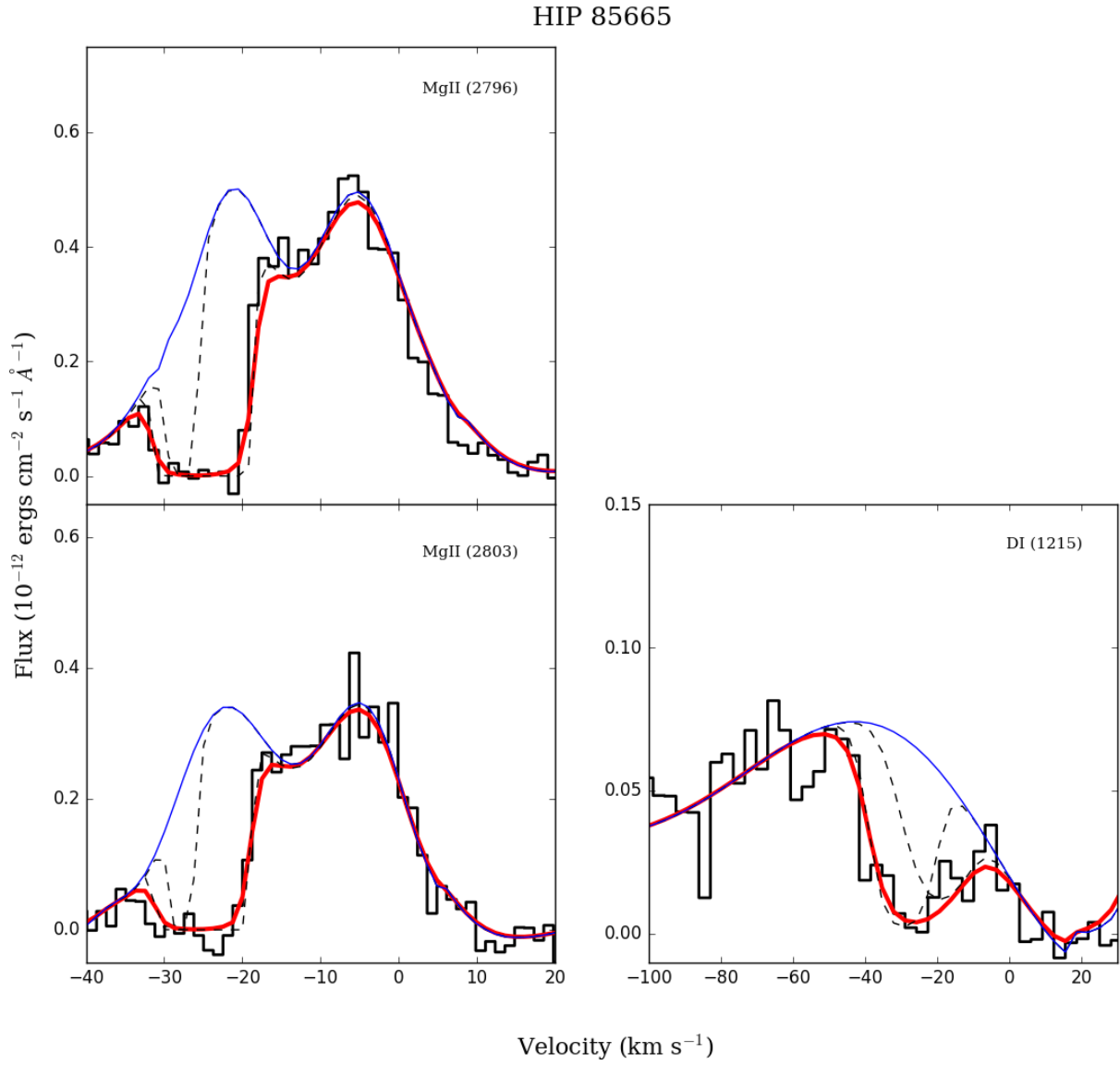


Figure 3.5: Same as Figure 3.3, but for the HIP 85665 sight line, where only MgII and DI showed ISM absorption.

3.4 Fit Parameters

The final parameters for each fit are presented in Tables 3.2–3.4. Listed for each component are the velocity (v [in km s^{-1}]), the Doppler parameter (b [in km s^{-1}]), and the column density ($\log N$ [in cm^{-2}]). For MgII and CII, the parameter values are the weighted mean from the individual and simultaneous fits. The associated errors are, in the case of multiple fits, either the standard deviation or the weighted mean errors, or the resulting Monte Carlo uncertainties if no simultaneous fit was performed.

Table 3.2: Fit parameters for GJ 780 components.

| Ion | Component # | v (km s ⁻¹) | b (km s ⁻¹) | log N (cm ⁻²) |
|-------------------|----------------|------------------------------|------------------------------|--------------------------------|
| DI ^c | 1 | -16.8 ± 1.6 | 6.0 ± 1.2 | 12.78 ± 0.25 |
| | 2 | -10.4 ± 2.9 | 7.1 ± 1.6 | 12.85 ± 0.32 |
| CII ^b | 1 | -18.88 ± 0.17 | 2.86 ± 0.38 | 14.11 ± 0.26 |
| | 2 | -9.56 ± 0.41 | 5.39 ± 0.60 | 13.98 ± 0.06 |
| CII* ^c | 1 | -18.88 ± 0.17 | 2.86 ± 0.38 | 12.37 ± 0.19 |
| | 2 | -9.56 ± 0.41 | 5.39 ± 0.60 | 11.28 ± 0.62 |
| OI ^c | 1 | -16.3 ± 1.3 | 2.26 ± 0.83 | 14.88 ± 0.59 |
| | 2 | -8.20 ± 0.64 | 2.62 ± 0.59 | 14.43 ± 0.34 |
| MgII | 1 | -15.91 ± 0.26 ^a | 3.39 ± 0.59 ^a | 12.88 ± 0.01 ^b |
| | 2 | -9.24 ± 0.11 ^b | 3.52 ± 0.10 ^b | 12.61 ± 0.02 ^a |

Table 3.3: Fit parameters for GJ 754 components.

| Ion | Component # | v (km s ⁻¹) | b (km s ⁻¹) | log N (cm ⁻²) |
|-----------------|----------------|------------------------------|------------------------------|--------------------------------|
| DI ^c | 1 | -27.4 ± 2.6 | 5.3 ± 1.3 | 13.19 ± 0.29 |
| | 2 | -18.5 ± 1.2 | 9.47 ± 0.45 | 13.17 ± 0.10 |

Table 3.4: Fit parameters for HIP 85665 components.

| Ion | Component # | v (km s ⁻¹) | b (km s ⁻¹) | log N (cm ⁻²) |
|-----------------|----------------|------------------------------|------------------------------|--------------------------------|
| DI ^c | 1 | -29.88 ± 0.88 | 7.65 | 13.52 ± 0.09 |
| | 2 | -20.3 ± 1.9 | 9.70 | 13.30 ± 0.11 |
| MgII | 1 | -29.47 ± 0.88 ^a | 1.51 ± 0.54 ^b | 12.72 ± 0.41 ^b |
| | 2 | -23.70 ± 0.66 ^b | 2.09 ± 0.47 ^b | 14.29 ± 0.34 ^b |

^aErrors are the standard deviation.^bErrors are the weighted mean uncertainties.^cErrors are Monte Carlo uncertainties.

Overall, for GJ 780 and HIP 85665, we find consistent ISM velocities in each different ion. We do note that they are not all the same as the MgII velocity, and we present a discussion of these offsets in Section 3.4.1. In general, as expected, the b values increase with decreasing atomic mass. HI and DI always have the largest Doppler parameters because they are dominated by thermal broadening. We see this same general result in our data. Additionally, our log column densities are very similar to average values measured by Redfield & Linsky (2008).

3.4.1 Velocity Offsets

We note that the component velocities for each ion in GJ 780 are not all the same as the MgII velocity, which we consider to be our baseline velocity. There are several reasons for these offsets. First, deuterium absorption is almost always very broad, which we can see in the high Doppler parameters. The uncertainties on the DI velocities account for this in that they are fairly large. We performed a quick test of the uncertainties by fitting the DI absorption with two components at the MgII velocities of -15.9 km s^{-1} and -9.2 km s^{-1} . The resulting fit was nearly identical to the best-fit model with the above DI velocities. There only were slight – within the 1σ errors of the other fit – changes to the Doppler parameters and column densities, which was expected.

When we consider the seemingly too-high velocity resulting from the CII fit, we also have to include consideration of the saturation in the line. Redfield & Linsky (2004a) found an average Doppler parameter of 3.64 km s^{-1} in their survey of stars within 100 pc that had high-resolution observations of interstellar FeII or MgII. While we report Doppler parameter values of $2.86 \pm 0.38 \text{ km s}^{-1}$ and $5.39 \pm 0.60 \text{ km s}^{-1}$ that are on either side of the average value, we note that

Redfield & Linsky (2004a) also had a wide range of CII Doppler parameters. For example, the η UMa CII spectrum showed evidence of strong saturation and, as such, Redfield & Linsky (2004a) recorded Doppler value of $6.16 \pm 0.71 \text{ km s}^{-1}$. Like the b value of our second component, this η UMa CII Doppler parameter is systematically high due to saturation in the line. Therefore, we think our higher radial velocity measurement is due to saturation. We also note that the uncertainties on the CII velocities are probably too low. Therefore, if we had reasonable uncertainties, we would likely consider the CII velocities to be within 3σ of the MgII velocities. Similarly, the difference between the OI component velocities and the MgII velocities is also due to saturation, but on a less significant scale.

We see similar offsets in the HIP 85665 velocities. However, we had to set the DI Doppler widths at fixed values in order to get `gismfit` to construct an accurate fit to the data. When left unconstrained, the Doppler parameters were slightly too high even for deuterium. We do note that the second DI component velocity is 1.8σ from its complementary MgII velocity and that this is not an unreasonable difference due to the uncertainties on the DI velocities.

3.4.2 Geocoronal Features

The Earth's atmosphere is constructed in layers, with the exosphere being the outermost and most tenuous. The exosphere begins at an altitude of around 500 km, and has been detected out to $\sim 15.5 R_{\odot}$ (Schultz 2014). It is composed of mostly neutral hydrogen atoms, and is detectable at UV wavelengths as a result of interactions with high energy photons from the Sun. Typically, we see substantial background emission due to HI. We often also detect absorption features in NI and

OI due to this terrestrial material (Redfield & Linsky 2004b). This absorption is usually easily identifiable because it is centered at the mean velocity of the Earth during the time of observation.

In the case of OI absorption in the GJ 780 spectrum, to yield a good fit to the data and get appropriate values for physical parameters, we had to force the OI b values to be at LISM average values. The b value of the second component (at -9 km s^{-1}) was chosen to be fixed at 3.24 km s^{-1} , the average for the OI b value (Redfield & Linsky 2004a). However, in order to get a Doppler parameter that was physically probable, we had to also fix the Doppler parameter of the first component at 6.70 km s^{-1} . This value is substantially higher than the average, but is not unprecedented given that Redfield & Linsky (2004a) measured a Doppler parameter of $6.63 \pm 2.99 \text{ km s}^{-1}$ for ι Cap. When the Doppler parameters were allowed to vary in order to reach the lowest possible χ^2 , as is the typical procedure when fitting absorption components, the second component Doppler parameter soared to the unphysical value of 8.2 ± 0.9 . Though we determine a decent fit to the data for the ISM absorption in OI, it was not ideal because of the fixed b values.

However, we were able to produce a far more excellent fit to the GJ 780 OI data when we included a geocoronal absorption feature. We used the IDL module `baryvel` to calculate the barycentric velocity of the Earth at the time observations of GJ 780 were taken with *HST*/STIS. `baryvel` outputs the barycentric velocity components of Earth in a right-handed coordinate system with the positive x-axis toward the Vernal Equinox and the positive z-axis pointed toward the North Celestial Pole.¹ Then, we projected the components of barycentric velocity along the line of sight toward GJ 780 using the celestial coordinates of the star. This

¹<https://idlastro.gsfc.nasa.gov/ftp/pro/astro/baryvel.pro>

gave the velocity ($v_r \approx -19.8 \text{ km s}^{-1}$) of the geocoronal component which was seen as an emission feature in HI, and as an absorption feature in the members of the OI multiplet. Once we had the velocity of the geocoronal component, we again used `gismfit` to perform a fit to the OI absorption. Instead of two components, like we used before, we included the geocoronal absorption as a third component with velocity $v_r \approx -19.8 \text{ km s}^{-1}$. Adding the third component decreased the Doppler parameters of the two ISM components to reasonable physical values ($2.26 \pm 0.83 \text{ km s}^{-1}$ and $2.62 \pm 0.59 \text{ km s}^{-1}$), and also resulted in the expected ISM velocities that were consistent with the MgII fits.

In Figure 3.6, we present both the DI line and Lyman α line of HI for GJ 754 and HIP 85665. The geocoronal emission can clearly be seen at around 50 km s^{-1} as a distinct peak. In Figure 3.7, we present the OI multiplet for GJ 780 with the geocoronal absorption feature velocity marked by the red line. ISM absorption is only seen in the 1302 \AA line. We can distinguish between geocoronal absorption and ISM absorption by looking at the other two lines of the multiplet. The OI 1304 \AA and 1306 \AA lines do not show any signs of ISM absorption, but the geocoronal velocity matches up perfectly with an absorption feature. We also show in Figure 3.8 that the geocoronal velocity for GJ 780 lines up with the geocoronal emission in HI.

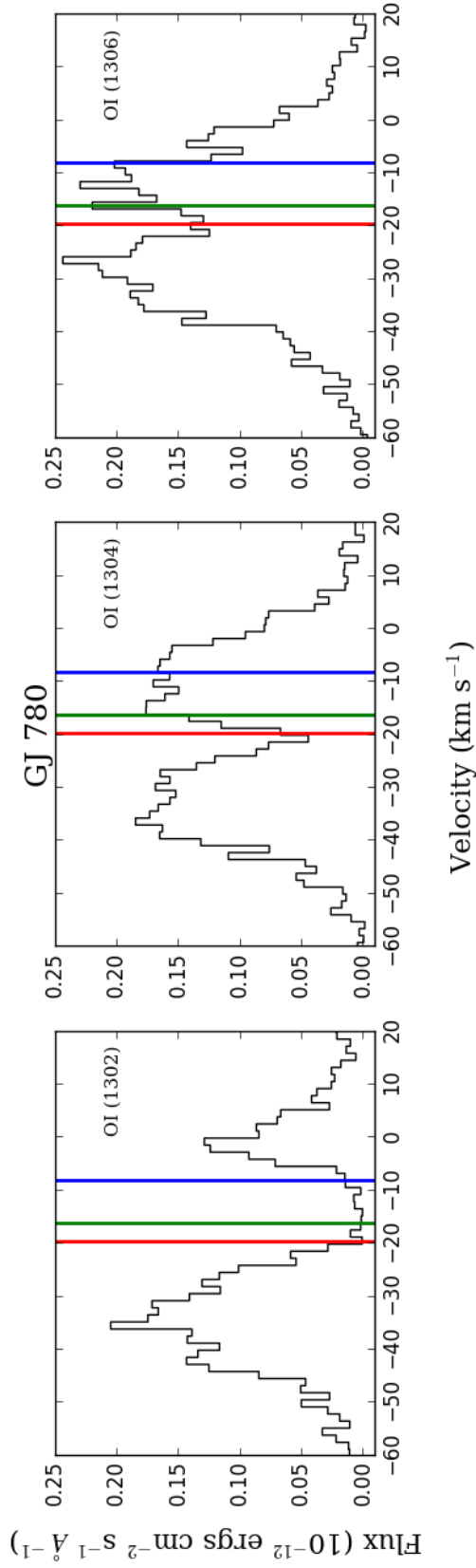


Figure 3.7: Same as Figure 3.6, but showing the OI multiplet of GJ 780 at 1302, 1304, and 1306 Å. The red line is the velocity of the geocoronal component, the green line is the velocity of the first absorption component, and the blue line is the velocity of the second absorption component.

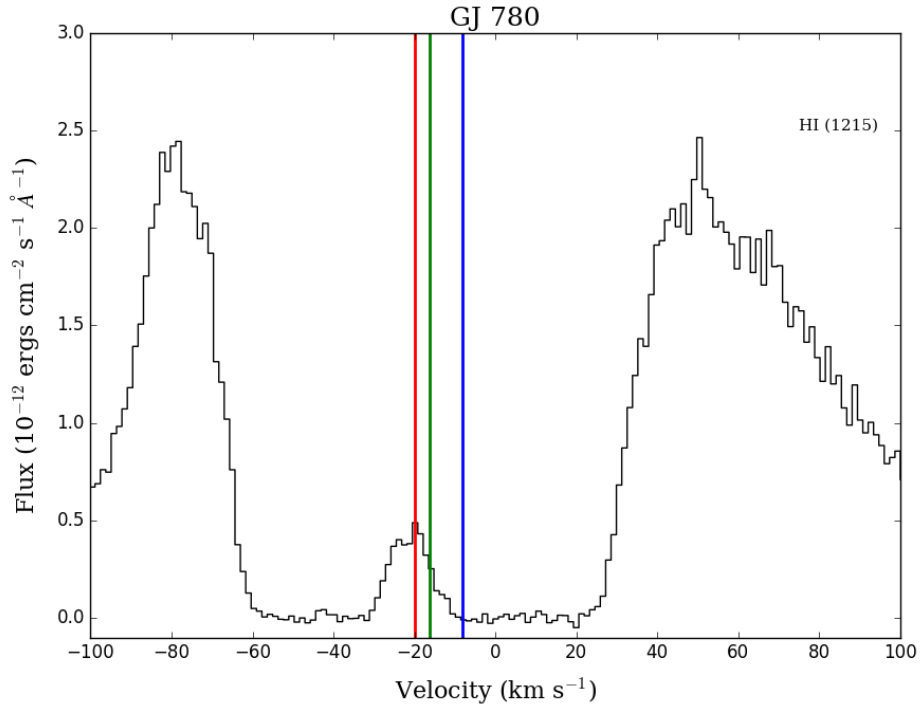


Figure 3.8: Same as Figure 3.6, but for the Lyman α line of HI.

3.5 The Lyman α Profile

The hydrogen Lyman α line is crucial to the study of solar and interstellar dynamics. The line is the first in the Lyman series of transitions, occurring at 1215.6700 Å. This wavelength is easily observed by *HST*/STIS, and we were therefore able to obtain high-resolution spectra of far-UV wavelength bands containing both the HI and DI Ly α lines. Interstellar hydrogen and deuterium atoms produce absorption features against the stellar Ly α line profile (Wood et al. 2005). These features are almost always strong enough to be observed for any sight line because hydrogen is so abundant, and ultimately provide important information about the LISM. Sometimes, in addition to the interstellar absorption, Ly α spectra show signs of absorption from the outer heliosphere or even from other

astrospheres (Wood et al. 2005). An astrosphere is the same structure as our heliosphere, but is one that occurs around other stars. The basic astrospheric model designed by Linsky & Wood (2014) includes a termination shock where the solar wind becomes subsonic, an astropause (analogous to the heliopause), and a hydrogen wall (H-wall), where inflowing neutral hydrogen accumulates and is heated by particle interactions. In the HI Ly α profile, the solar H-wall appears as extra absorption red-ward of the LISM absorption, while a stellar H-wall would appear blue-ward of the LISM absorption (Linsky & Wood 2014).

Before we can even model the missing stellar continuum, we have to remove the geocoronal emission. Because the geocoronal emission is relatively narrow and contained within the saturated core of HI, it can be approximated by fitting a simple Gaussian profile with `gismfit` and then subtracting it out from the data (Wood et al. 2005). The geocorona also can act as a wavelength calibrator. The data reduction is done in a heliocentric rest frame, which means that the geocoronal emission is at a velocity that is the projected barycentric velocity of Earth at the same time. We can then compare the calculated `baryvel` velocity with the actual emission line center and determine if an offset exists. In order to determine the sources of absorption, we must first reconstruct the unknown stellar emission line (Linsky & Wood 1996). This is particularly difficult to do because the hydrogen Ly α line is broad and often saturated. We can see in Figure 3.4 that the absorption in HI Ly α is indeed extremely broad – spanning at least 80 km s^{-1} in velocity space – and definitely saturated. The saturation stems from not only the high abundance of neutral hydrogen atoms in the LISM, but also the high oscillator strength of hydrogen. HI column densities even for short sight lines are high enough that the absorption profile has extended damping wings (Wood et al. 2005). This just adds another level of complexity to the profile reconstruction, but

it just so happens that our fits to the DI Ly α line can provide initial conditions for reconstructing the HI profile. The DI absorption fit should indicate what the central wavelength and Doppler width would be for HI (Wood et al. 2005). The HI absorption should have the same centroid velocity as deuterium, and the two Doppler parameters are related by $b(\text{HI}) \approx \sqrt{2}b(\text{DI})$. This equation allows us to compute a Voigt opacity profile, τ_λ for HI based on various assumed values for hydrogen column density (Wood et al. 2005). This profile can effectively reconstruct the “wings” of the HI Ly α line when we multiply the data by $\exp(\tau_\lambda)$.

To reconstruct the rest of the profile we consider the MgII *h* and *k* lines. Both Ly α and the MgII doublet are optically thick chromospheric lines that have similar profiles when seen in the solar spectrum (Wood et al. 2005). The stellar continua for both MgII and Ly α will often be the same shape, and therefore we can use the MgII lines to reconstruct the HI Ly α profile. The program `lymangauss`, written by E. Edelman, uses a certain number of Gaussians to approximate the double-peaked shape of the MgII lines and then places the new continuum over the center of the Ly α line. In Figure 3.9, we present an initial reconstruction of the HI Ly α in GJ 780. Note that this is a preliminary, reconstruction with the final fit to be completed in the future.

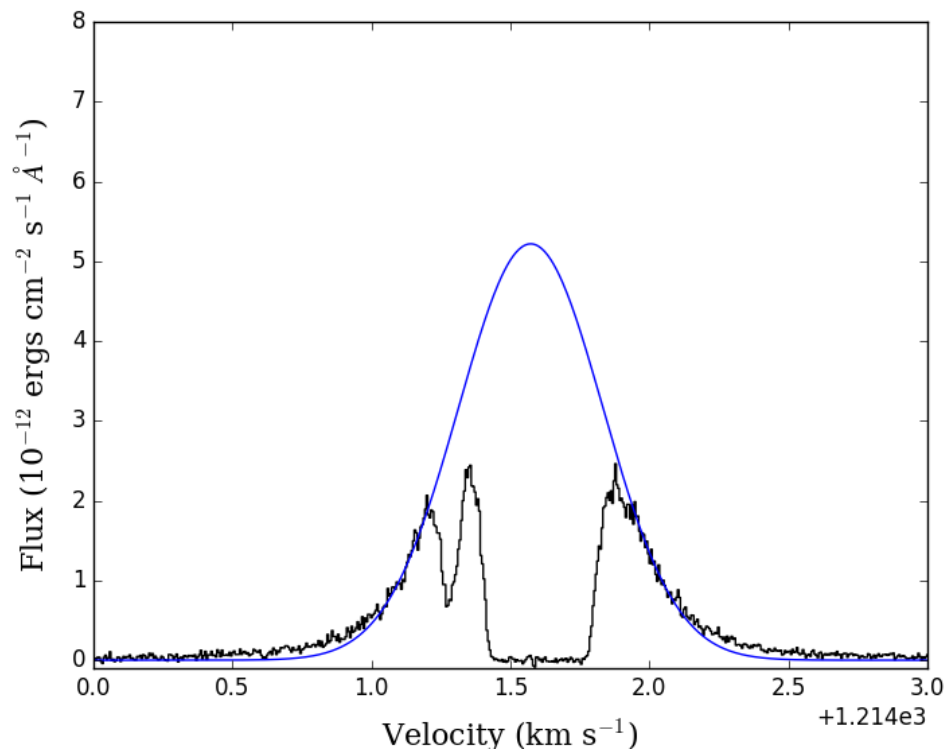


Figure 3.9: Initial reconstruction of the HI Ly α profile in GJ 780. The black histogram is the observed flux data. The blue line is a simple Gaussian intended to represent the missing stellar continuum.

Chapter 4

Analysis of Physical Parameters

The ISM fit parameters can be used to measure the physical properties of the LISM. We hope that these physical constraints will allow us to identify the interstellar clouds that are the sources of the absorption we see. Ultimately, we want to characterize the LISM through which the *Voyager* spacecraft will eventually travel and connect our derived measurements to those measured in situ by the spacecraft.

4.1 Comparing with the Kinematic Model

In Section 3.4, we presented our calculated radial velocity values for each of the ISM absorption components for three sight lines. We now include in greater detail a discussion of how well our velocities match known LISM cloud velocities. Redfield & Linsky (2008) provide an online LISM Dynamical Model Kinematic Calculator,¹ which calculates which LISM clouds are traversed for any sight line given the coordinates of that sight line. The Kinematic Calculator also calculates the radial and transverse velocities for each of the 15 clouds in the model developed by Redfield & Linsky (2008). In the following table, we present a comparison between our radial velocities and those from the Kinematic Calculator.

¹<http://lism.wesleyan.edu/LISMdynamics.html>

Table 4.1: Comparison with LISM Dynamical Model.

| Gliese # | Other Name | Distance (pc) | Component # | v (km s ⁻¹) | Cloud | Alternative Explanation |
|------------------------|------------|---------------|-------------|----------------------------|-------|-------------------------|
| <i>Voyager 1</i> | | | | | | |
| GJ 678.1A ^a | HIP 85665 | 9.98 | 1 | -29.68 ± 0.62 ^c | Oph | |
| | | | 2 | -23.4 ± 2.4 ^b | LIC | |
| <i>Voyager 2</i> | | | | | | |
| GJ 780 ^a | δ Pav | 6.11 | 1 | -18.0 ± 1.3 ^b | Vel | |
| | | | 2 | -9.23 ± 0.90 ^b | Dor | |
| GJ 754 | LHS 60 | 5.91 | 1 | -27.4 ± 2.6 ^d | Vel | G, Mic(?) |
| | | | 2 | -18.5 ± 1.2 ^d | G | Aql(?) |

^aVelocity is the weighted mean of the velocities found for each ion.

^bErrors are the standard deviation.

^cErrors are the weighted mean uncertainties.

^dErrors are Monte Carlo uncertainties.

One important feature of the Kinematic Calculator is that it not only returns the projected velocity vectors for all 15 clouds, but also lists which clouds are traversed by the sight line, which clouds are within $<20^\circ$ of the sight line, and which clouds are far ($>20^\circ$) from the sight line. We were able to predict which clouds correspond to each ISM absorption component based off the both the velocity vectors and if a cloud traverses the sight line or not. If more than one cloud is a possible match to the component velocity, it is listed under “Alternative Explanation.”

4.1.1 The *Voyager 1* Sight Line

Though we only were able to calculate velocities for one target star along the *Voyager 1* sight line, we actually find that these velocities match up quite well with known ISM cloud velocities. HIP 85665 has the smallest angular separation $\Delta\theta$ from the *Voyager 1* sight line, indicating a strong likelihood that whatever clouds we identify along its path will intersect with the path of *Voyager 1*. The first absorption component has a velocity of $-29.68 \pm 0.62 \text{ km s}^{-1}$, which is nearly identical to the predicted velocity for the Oph cloud ($v_r = -29.66 \pm 0.64 \text{ km s}^{-1}$). Therefore, we are confident that we see absorption from the Oph cloud along the *Voyager 1* line of sight.

The second component is slightly more ambiguous. The averaged velocity of $-23.4 \pm 2.4 \text{ km s}^{-1}$ is only 0.5σ away of the velocity of the LIC cloud, which is $-22.15 \pm 0.99 \text{ km s}^{-1}$. However, we note that the higher velocity could indicate contamination from other clouds that traverse the *Voyager 1* sight line to HIP 85665. The Mic cloud is also traversed by this sight line, and it has a velocity of $-27.05 \pm 0.98 \text{ km s}^{-1}$. The G cloud falls within 20° of this line of sight, and also has a velocity around -27 km s^{-1} . It is entirely possible that we see some minor

absorption from one or both of these two nearby clouds. However, we believe that the component velocity matches up well with the LIC.

4.1.2 The *Voyager 2* Sight Line

Unlike the *Voyager 1* sight line, the *Voyager 2* sight line is a bit more complicated. We have absorption component velocities for both target stars – GJ 754 and GJ 780 – but the uncertainty on the GJ 754 component velocities are considerably higher than those of GJ 780. We were only able to detect ISM absorption in DI, and as such, the constraints on the velocity values are looser than those determined by examining the MgII doublet. Despite falling within 15° of the direct *Voyager 2* line of sight, GJ 780 and GJ 754 are actually greater than 20° away from each other. This large distance discrepancy between the two targets lends some uncertainty to which clouds occur on the path of *Voyager 2*.

With a velocity of $-18.0 \pm 1.3 \text{ km s}^{-1}$, the first component of GJ 780 matches up closely with the velocity of the Vel cloud ($v_r = -18.71 \pm 1.09 \text{ km s}^{-1}$). According to the Kinematic Calculator, the *Voyager 2* sight line to GJ 780 directly traverses the Vel cloud. The other clouds to which the sight line passes near all have velocities that could not sufficiently explain the velocity measured for the first absorption component. The discrepancy between the measured velocity and the Kinematic Calculator-based velocity is not larger than either of the associated uncertainties. We therefore are confident that we see absorption from the Vel cloud in the first component of GJ 780.

The second observed absorption component of GJ 780 also appears to nearly match with an identified cloud. The Kinematic Calculator indicates that the Dor cloud passes near ($<20^\circ$) the *Voyager 2* line of sight with a velocity of $-8.62 \pm$

0.60 km s⁻¹. We find that the second component has a velocity of -9.23 ± 0.90 km s⁻¹. This component velocity is consistent with the velocity of the Dor cloud to $<1\sigma$, which indicates that it is a good match.

The velocities of the two components of GJ 754 are more difficult to match with known ISM clouds. Not only are the uncertainties higher, but also the absorption we see could be from more than one cloud. The *Voyager 2* sight line to GJ 754 directly traverses the Aql cloud and passes within 20° of the G, Mic, and Vel clouds. However, though the first component's velocity of -27.4 ± 2.6 km s⁻¹ is not consistent with the Aql cloud velocity, it is only 1.5σ away from that of the Vel cloud ($v_r = -31.89 \pm 1.52$ km s⁻¹). That the first absorption component velocity is lower than the velocity of the Vel cloud could indicate contaminant absorption by the G or Mic clouds ($v_r = -20.55 \pm 1.51$ km s⁻¹ and $v_r = -21.68 \pm 1.19$ km s⁻¹, respectively). It is more likely that the velocities of both the first and second absorption components would be better constrained if we had ISM absorption in the Mg II *h* and *k* lines. Because we do not, the values from absorption in DI are fairly ambiguous.

Similarly, the second component of GJ 754 has a velocity of -18.5 ± 1.2 km s⁻¹, which is in between the velocities of the G and Aql clouds. It falls about 1.9σ away from the velocity of the G cloud, indicating that the G cloud is likely a primary source of the observed absorption. We cannot definitively rule out that we see some absorption from the Aql cloud because it lies directly along the line of sight to GJ 754.

4.2 Temperature and Turbulence

Since we have measurements of Doppler parameters resulting from the fits, we can derive estimates for temperature and turbulence of the ISM along the lines of sight. The equation that illustrates the relationship between Doppler parameter (b [km s⁻¹]), temperature (T [K]), and turbulent velocity (ξ [km s⁻¹]) is

$$b^2 = \frac{2kT}{m} + \xi^2 = 0.01662 \frac{T}{A} + \xi^2, \quad (4.1)$$

where k is the Boltzmann constant, m is the mass of the observed ion, and A is the atomic weight of the element (Redfield & Linsky 2004b). It is possible to solve Equation 4.1 for temperature and turbulence with only two line width components. However, the two ions must have very different atomic weights in order for this to yield accurate measurements (Redfield & Linsky 2004b). While it would be best to use the two ions that have the greatest mass difference, hydrogen and iron, we do not have any value on the Doppler parameter for any iron lines. Instead, MgII can be used as a proxy for iron because it is the next heaviest commonly detected ion. For GJ 780, we have, for both absorption components, four different ions – MgII, CII, OI, and DI – we can use. DI is the next lightest ion after HI and is typically unsaturated for short sight lines, therefore providing a reliable Doppler parameter for measurement (Redfield & Linsky 2004b).

We present four plots, Figures 4.1-4.4, for GJ 780 and HIP 85665 visualizing the temperature and turbulent velocity determination. The values and associated uncertainties were calculated and then plotted using the IDL routine `plot_temp`. We also present, in Table 4.2, both the parameters that were used to calculate temperature and turbulence and the results from the calculated values.

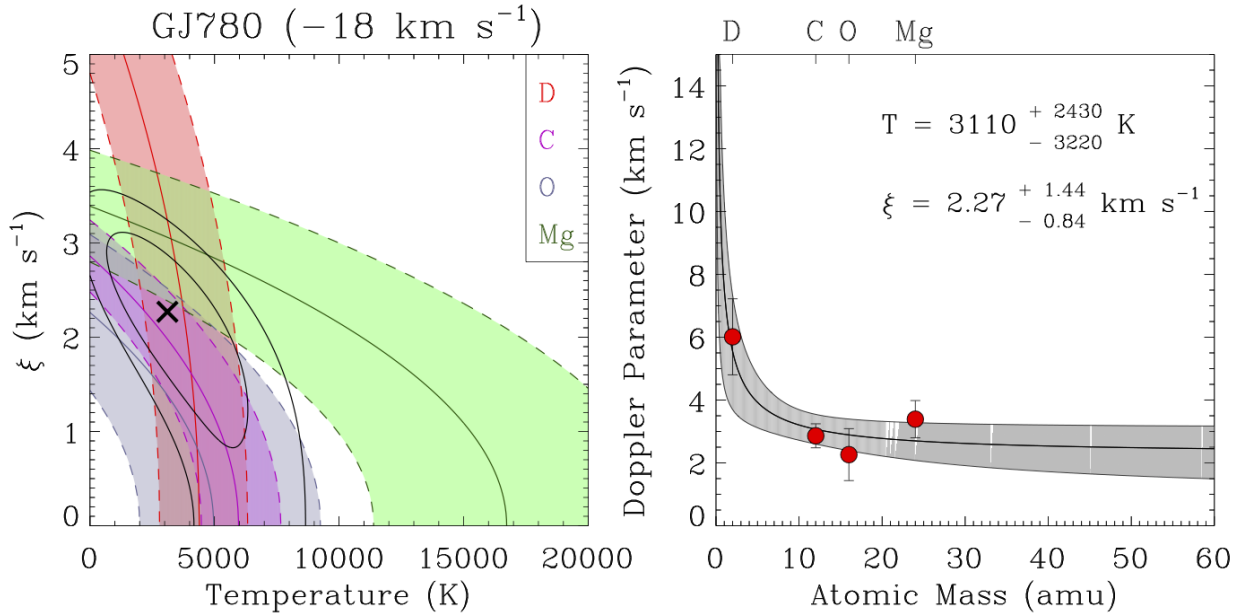


Figure 4.1: The left-side plot shows temperature versus turbulent velocity for a given Doppler parameter of a particular ion. The colors indicate the ion. For example: deuterium is red, carbon is purple, oxygen is blue, and magnesium is green. The colored dashed lines are $\pm 1\sigma$ errors around the solid line, which is from Equation 4.1, yielding an individual best-fit curve in the temperature-turbulence plane (Redfield & Linsky 2004b). The black cross is the best-fit value of the temperature and turbulent velocity based on the measured Doppler parameters. The black contours are 1 and 2σ errors for both values (Redfield & Linsky 2004b). The right-side plot shows Doppler parameter plotted against the atomic mass of the ions. The red symbols are the observed Doppler parameter values and associated uncertainties from the data. The solid line is the best-fit curve given from Equation 4.1. The shaded region includes all fits within the 1σ contours from the left-side plot.

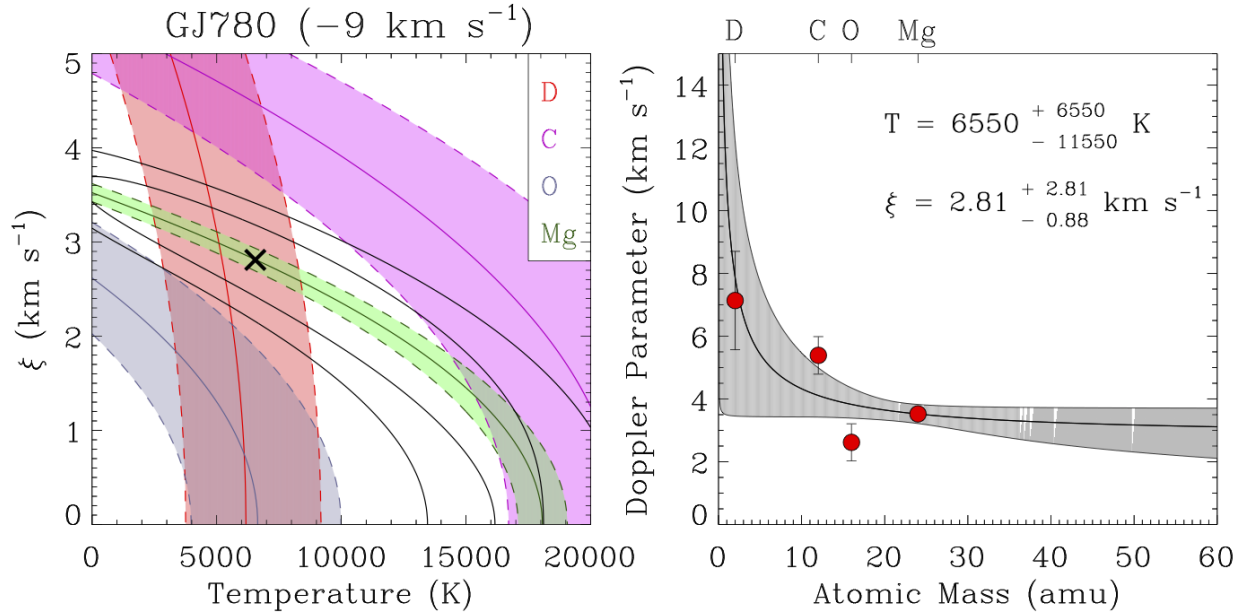


Figure 4.2: Same as Figure 4.1, but for the -9 km s^{-1} component of GJ 780.

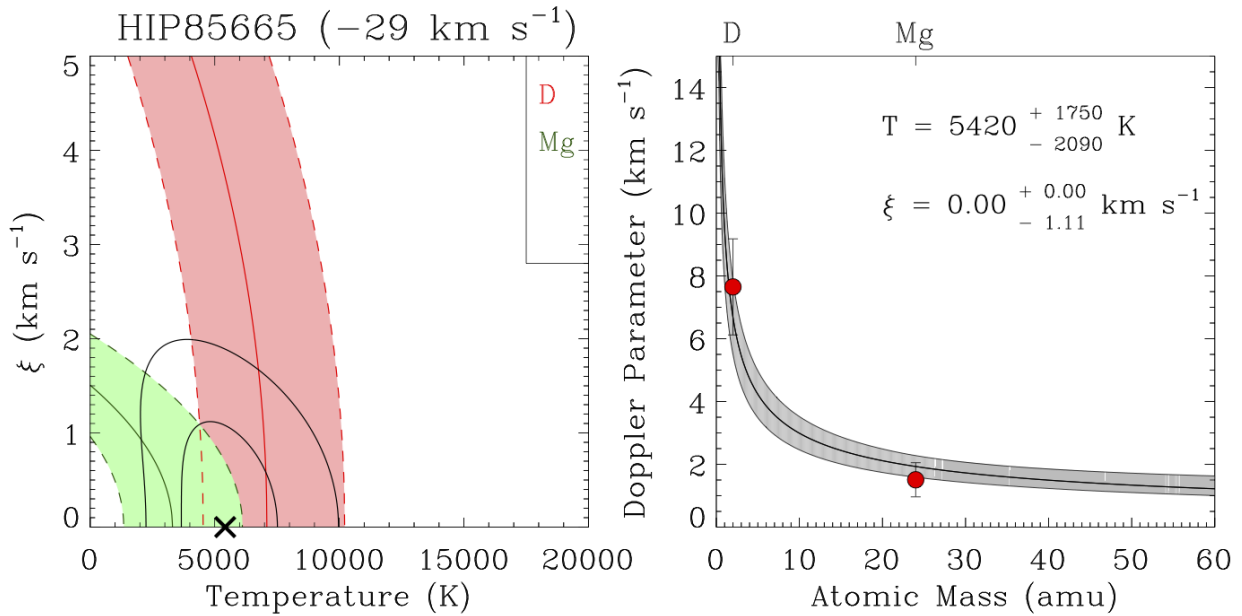


Figure 4.3: Same as Figure 4.1, but for the -29 km s^{-1} component of HIP 85665 without carbon or oxygen.

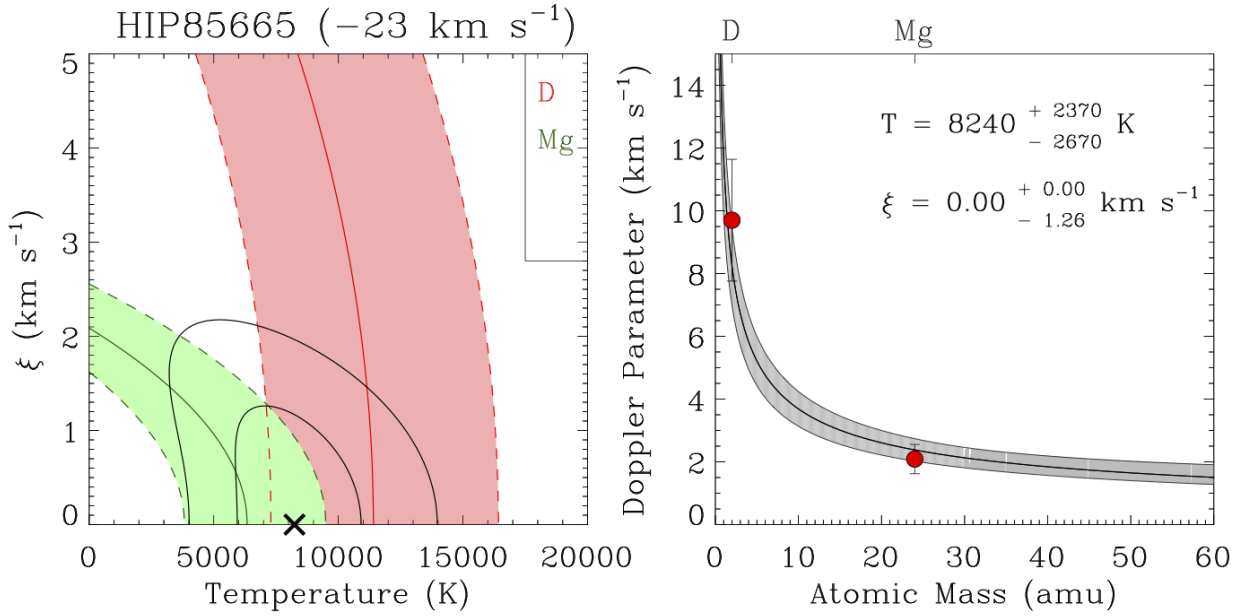


Figure 4.4: Same as Figure 4.1, but for the -23 km s^{-1} component of HIP 85665 without carbon or oxygen.

Table 4.2: Temperature and turbulence values for GJ 780 and HIP 85665.

| Gliese # | Other Name | Component # | v (km s $^{-1}$) | T (K) | ξ (km s $^{-1}$) |
|-----------|--------------|-------------|---------------------|-------------------------|------------------------|
| GJ 780 | δ Pav | 1 | -18.0 ± 1.3 | 3110^{+2430}_{-3220} | $2.27^{+1.44}_{-0.84}$ |
| | | 2 | -9.23 ± 0.90 | 6550^{+6550}_{-11550} | $2.81^{+2.81}_{-0.66}$ |
| GJ 678.1A | HIP 85665 | 1 | -29.68 ± 0.62 | 5420^{+1750}_{-2090} | $0.00^{+0.00}_{-1.11}$ |
| | | 2 | -23.4 ± 2.4 | 8420^{+2370}_{-2670} | $0.00^{+0.00}_{-1.26}$ |

Now that we have identified the most likely ISM clouds from which we measure the velocities of absorption components, we can begin to make comparisons between our derived temperatures and turbulences and the averaged measurements for specific clouds calculated by Redfield & Linsky (2008).

We are confident that we see absorption in the two components along the *Voyager 2* line of sight (GJ 780) from the Vel and Dor clouds, respectively. Redfield & Linsky (2008) do note that there was only one sight line with physical measurements for each cloud, and that their measured values are uncertain. We are confident in our measurement for the temperature and turbulence of the Vel cloud after adjusting the OI fit to include the geocoronal absorption component. We find a temperature of 3110_{-3220}^{+2430} K and a turbulence of $2.27_{-0.84}^{+1.44}$ km s⁻¹. Our temperature is vastly different than what was derived by Redfield & Linsky (2008), but this discrepancy between our measured temperature and the Redfield & Linsky (2008) temperature of 10600 K is due to the uncertainty in their measurement. With further measurements along additional Vel lines-of-sight, we could certainly better constrain the temperature. Their turbulence ($\xi = 3.5$ km s⁻¹) is 0.85σ from our value. Again, additional observations would be necessary to tighten the uncertainties and solidify the average value for Vel.

The second component, which we identify as the Dor cloud, has a temperature of 6550_{-11550}^{+6550} K, which is very close to the Redfield & Linsky (2008) temperature of 7000K. However, we have to consider that the error bars on the second component temperature are extremely large. We acknowledge that the below-zero lower limit is likely an artifact of the fitting routine, and should not be considered to be a real temperature value. Likewise, the turbulence we find ($\xi = 2.81_{-0.66}^{+2.81}$ km s⁻¹) is 0.95σ from the average Dor turbulence of 5.5 km s⁻¹. However, we can see from the left-side panel in Figure 4.2 that the CII and OI best-fit curves to the

temperature-turbulence plane to not match up well with the best-fit value. This is likely because the absorption components were saturated, and we could not obtain an entirely accurate estimate the respective Doppler parameters. However, we do see that the Doppler parameters for both CII and OI are reasonably close to the best-fit curve plotted in the right-side panel of Figure 4.2.

While the temperatures of the two HIP 85665 components are reasonable, the turbulence values are somewhat unrealistic. Both turbulences have a best-fit value of 0 km s^{-1} . We can see from Figures 4.3 and 4.4 that the 1 and 2σ contours indicate the possibility of having positive turbulence. A probable cause for the turbulence values being what they are is that we only have two Doppler parameter values available for fitting. This likely reduces the certainty with which we can constrain our additional physical parameters. We are confident in our conclusion made in Section 4.1 that we see absorption from the Oph and LIC clouds in our first and second absorption components, respectively. However, the average turbulences ($\xi_{\text{Oph}} = 3.3 \text{ km s}^{-1}$ and $\xi_{\text{LIC}} = 1.62 \pm 0.75 \text{ km s}^{-1}$) are nowhere near the values we derive. Despite the large discrepancies in turbulence, the temperature values for both components match up reasonably well with their respective averages from Redfield & Linsky (2008). Like the Vel and Dor clouds, the Oph cloud only has one line of sight for which physical measurements could be made (Redfield & Linsky 2008). We take this uncertainty into account, and therefore find that our temperature of $5420_{-2090}^{+1750} \text{ K}$ is reasonable for the Oph cloud. Luckily, Redfield & Linsky (2008) have 79 total sight lines for the LIC, with 19 of those used to calculate an average temperature of $7500 \pm 1300 \text{ K}$. Our temperature value of $8240_{-2670}^{+2370} \text{ K}$ is similar to temperatures measured along other LIC sight lines, and is relatively close to the average temperature. Based on the wide range of LIC temperatures, we conclude that our temperature coincides well

with other LIC sight line temperatures.

4.3 Abundance and Depletion

As previously discussed in Section 1.3.3, depletion occurs when heavy elements have gas phase abundances that are less than the expected cosmic abundances, presumably due to incorporation into dust. Depletion is calculated from

$$\log(X_{\text{gas}}/H) = \log(N(X)/N(H)) - \log(X/H)_{\odot}, \quad (4.2)$$

where X denotes the heavier element, $N(X)$ is the column density of that element, and H is hydrogen (Jenkins 2009). Equation 4.2 indicates that the depletion is determined by first calculating the ISM abundances and then subtracting the solar abundances (Wood et al. 2002). Hydrogen abundance is calculated from the deuterium column density and then converted to hydrogen by using a deuterium-to-hydrogen ratio (hereafter, D/H) (Redfield & Linsky 2008). The most accurate LISM D/H ratio was calculated by Linsky et al. (2006), who used measurements of D/H from the *Far Ultraviolet Spectroscopic Explorer (FUSE)*, *HST*, *Copernicus*, and the *Interstellar Medium Absorption Profile Satellite (IMAPS)*. They determined that the D/H ratio of $(1.56 \pm 0.4) \times 10^{-6}$ is consistent for column densities $\log[N(H)] < 19.2$. This column density is indicative of ISM inside the Local Bubble. Because all four of our target stars are within 20 pc of Earth, they lie well within the edge of the Local Bubble (~ 50 pc). As such we use the Linsky et al. (2006) D/H ratio to convert from $N(DI)$ to $N(H)$. We also adopt solar abundances and the associated uncertainties from Asplund et al. (2009). The error on the results from Equation 4.2 was calculated by error propagation based on the uncertainties on $\log N(X)$ and $\log X_{\odot}$.

We present in Table 4.3 gas and dust depletions for MgII, CII, and OI in GJ 780, and in Table 4.3 MgII depletion toward HIP 85665. The “X” in the header of each table denotes the respective element according to the Ion column.

The most notable result from these calculations is that most of these ions appear to be locked in dust - that is, their respective abundances are high for dust and low for gas. We see that the dust column densities are higher than the gas column densities given in Tables 3.2–3.4. Like in Section 4.2, we can also make a general comparison to depletion values calculated by Redfield & Linsky (2008). We see absorption from two component clouds, Vel and Dor, along the GJ 780 sight line. Unfortunately, we find that neither of our magnesium depletion values (-1.30 ± 0.004 and -1.65 ± 0.004 , respectively) match up with those measured by Redfield & Linsky (2008) along the Vel and Dor lines of sight. However, just as mentioned in Section 4.2, we keep in mind that their values are highly uncertain. We find that their depletions for both clouds – $\langle D(\text{Mg}) \rangle_{\text{Vel}} = -0.03$ and $\langle D(\text{Mg}) \rangle_{\text{Dor}} = -0.65$ – are significantly different from our depletions.

Likewise, the magnesium depletion of the first component in HIP 85665, from the Oph cloud, does not match up at all with the measurement from Redfield & Linsky (2008). Again, Redfield & Linsky (2008) only had one sight line with physical measurements for the Oph cloud, but regardless, our value of -2.206 ± 0.004 is nowhere near their measurement of -0.84 ± 0.34 . It is entirely possible that we are seeing a different part of the cloud than was observed by Redfield & Linsky (2008), but without further confirmation from other physical measurements, we cannot definitively conclude on this comparison. However, the magnesium depletion of the second component from the LIC matches up reasonably well with the average value from Redfield & Linsky (2008). Our value of -0.423 ± 0.004 is

Table 4.3: GJ 780 and HIP 85665 depletion values.

| Ion | Component # | $\log N(X)_{\text{gas}}$ ($\log \text{cm}^{-2}$) | $\log N(\text{H})$ ($\log \text{cm}^{-2}$) | $\log X_{\odot}^{\text{a}}$ | $\log X_{\text{gas}}/\text{H}$ | $\log N(X)_{\text{dust}}$ ($\log \text{cm}^{-2}$) |
|-----------|-------------|---|---|-----------------------------|--------------------------------|--|
| GJ 780 | | | | | | |
| CII | 1 | 14.11 ± 0.26 | 18.59 ± 0.25 | 8.43 ± 0.05 | -0.88 ± 0.01 | 14.96 ± 0.25 |
| | 2 | 13.98 ± 0.06 | 18.66 ± 0.32 | ... | -1.11 ± 0.01 | 15.05 ± 0.32 |
| OI | 1 | 14.62 ± 0.14 | 18.59 ± 0.25 | 8.69 ± 0.05 | -0.65 ± 0.01 | 15.17 ± 0.25 |
| | 2 | 14.03 ± 0.57 | 18.66 ± 0.32 | ... | -1.32 ± 0.01 | 15.33 ± 0.32 |
| MgII | 1 | 12.88 ± 0.01 | 18.59 ± 0.25 | 7.60 ± 0.04 | -1.30 ± 0.004 | 14.16 ± 0.25 |
| | 2 | 12.61 ± 0.02 | 18.66 ± 0.32 | ... | -1.65 ± 0.004 | 14.25 ± 0.32 |
| HIP 85665 | | | | | | |
| MgII | 1 | 12.72 ± 0.41 | 19.33 ± 0.09 | 7.60 ± 0.04 | -2.206 ± 0.004 | 14.93 ± 0.10 |
| | 2 | 14.29 ± 0.34 | 19.11 ± 0.11 | ... | -0.423 ± 0.004 | 14.50 ± 0.11 |

^aWhere $\log H_{\odot} = 12$

at the lower edge compared to the range of values the authors measured for the LIC. It happens that our depletion is 2.4σ from their average of -0.97 ± 0.23 . A possible explanation for this slightly lower magnesium depletion is the sheer size of the LIC. It covers approximately 18300 deg^2 across the sky, which is an extremely vast area compared to other ISM clouds (see Figure 1.5). The fact that the LIC is so large may allow for such discrepancies between individual sight line measurements.

4.4 Electron Density

One of the most important measurements we were able to make was to derive a value for electron density along the *Voyager 2* sight line. Because both *Voyager* spacecraft are still capable of measuring electron density with the Plasma Wave System², we can compare our derived electron density value with their in situ measurements. Redfield & Falcon (2008) measured electron densities (n_e) using the ratio of the collisionally excited CII line column density to the resonance CII line column density. The excited carbon line is a fine-structure doublet. Fine-structure describes how spectral lines of atoms split into degenerate multiplets from relativistic corrections leading to a small shift in energy on the order of $10^{-4} - 10^{-5} \text{ eV}$. The presence of these fine structure lines in the ISM gives density information of the absorbing medium (Bahcall & Wolf 1968). Densities derived from the collisionally excited lines do not depend on the radiation field, which is why they are used (Frisch et al. 2011). The resonance absorption line at 1334.5323 \AA corresponds to the transition from the ground state at $J = \frac{1}{2}$, while the CII excited absorption line doublet (1335.6627 and 1335.7077 \AA) represents the tran-

²<https://nssdc.gsfc.nasa.gov/nmc/experimentDisplay.do?id=1977-084A-13>

sition from the excited state of the fine-structure doublet at $J = \frac{3}{2}$ (Bahcall & Wolf 1968; Redfield & Falcon 2008). Electron collisions are responsible for populating the excited state, and therefore, the ratio of the column densities is proportional to the electron density by

$$\frac{N(\text{CII}^*)}{N(\text{CII})} = \frac{n_e C_{12}(T)}{A_{21}}. \quad (4.3)$$

The relation given in Equation 4.3 is derived from thermal equilibrium between collisional excitation of the fine-structure doublet and total radiative de-excitation (Redfield & Falcon 2008). In Equation 4.3, $N(\text{CII}^*)$ and $N(\text{CII})$ are the column densities of the excited line and resonance line, respectively, and $A_{21} = 2.29 \times 10^{-6} \text{s}^{-1}$ is the radiative de-excitation rate coefficient (Nussbaumer & Storey 1981). The collision rate coefficient $C_{12}(T)$ can be written as

$$C_{21}(T) = \frac{8.63 \times 10^{-6} \Omega_{12}}{g_1 T^{0.5}} \exp\left(-\frac{E_{12}}{kT}\right), \quad (4.4)$$

where $g_1 = 2$ is the statistical weight of the ground state and $E_{12} = 1.31 \times 10^{-14}$ ergs is the energy of the transition. Like Redfield & Falcon (2008), we adopt the value of $\Omega_{12} = 2.81$, and initially assumed a temperature of $T = 7000$ K.

We were fortunate in that the GJ 780 spectra contained ISM absorption in CII and collisionally excited CII*. We followed the fitting procedure outlined by Redfield & Falcon (2008), but we were unable to perform an individual fit to the excited line alone. The ISM absorption in CII* was present, but proved exceedingly difficult to fit on its own. Instead, we performed a fit to the resonance line, and then recreated the missing stellar flux for the excited line before finally performing a simultaneous fit to both lines. We were able to successfully fit to

both lines, and find well-constrained values for column density. We note that the dominant source of systematic error comes from the saturation of the CII resonance line, which is indicated by the high ($\sim 5 \text{ km s}^{-1}$) Doppler parameter of the second ISM component (see Table 3.2). This saturation results from high CII abundances and a high atomic oscillator strength (Frisch et al. 2011).

Using Equations 4.3 and 4.4, we were able to derive values for electron density for both ISM absorption components in GJ 780. These values are presented in Table 4.5. Table 4.5 not only includes the n_e values for the initial temperature of $T = 7000 \text{ K}$, but also values for n_e using the upper limits and median values for the temperatures calculated in Section 4.2. The uncertainties on n_e were calculated using simple rules of error propagation based on the initial uncertainties on the column densities. In particular, we note that the different temperatures do not change the electron density by much.

Table 4.4: GJ 780 electron densities.

| Component # | v (km s^{-1}) | $\log N(\text{CII}^*)$ (cm^{-2}) | $\log N(\text{CII})$ (cm^{-2}) | T (K) | n_e (cm^{-3}) |
|----------------|-------------------------------|--|--|------------|-------------------------------|
| 1 | -18.0 ± 1.3 | 12.37 ± 0.19 | 14.11 ± 0.26 | 7000 | 0.29 ± 0.21 |
| | ... | ... | ... | 3110 | 0.20 ± 0.15 |
| | ... | ... | ... | 5540 | 0.26 ± 0.19 |
| 2 | -9.23 ± 0.90 | 11.28 ± 0.62 | 13.98 ± 0.06 | 7000 | 0.03 ± 0.05 |
| | ... | ... | ... | 6550 | 0.03 ± 0.04 |
| | ... | ... | ... | 13100 | 0.04 ± 0.06 |

4.4.1 Comparisons to *Voyager*

In April 2013, shortly after it crossed the heliopause, *Voyager 1*'s Plasma Wave System detected locally-generated electron plasma oscillations at a frequency of about 2.6 kHz (Gurnett et al. 2013). Electron plasma oscillations occur at the electron plasma frequency, a characteristic frequency of

$$f_p = 8980\sqrt{n_e}, \quad (4.5)$$

where frequency has units of Hertz. The oscillations are excited by electron beams such as those upstream of interplanetary or interstellar shocks or after energetic solar outbursts (Gurnett et al. 2013). The *Voyager* spacecraft last observed electron plasma oscillations in 2004 (*V1*) and 2007 (*V2*) when just upstream of the heliospheric termination shock. Gurnett et al. (2013) obtained a series of short samples of the electric field waveform and used Fourier analysis techniques to convert the waveforms into frequency-time spectrograms, as shown in Figure 4.5.

Using Equation 4.5, Gurnett et al. (2013) calculated that the frequency of 2.6 kHz corresponded to an electron density of $n_e = 0.08\text{cm}^{-3}$. Gurnett et al. (2013) also discovered that the densities observed by *Voyager 1* are gradually increasing with radial distance at about 19% per AU. The observed electron densities are well within the range of remote-sensing measurements of plasma densities (0.06–0.21 cm^{-3}) in the LISM (Redfield & Falcon 2008). Based on *Voyager 2* Plasma Wave System measurements out to ~ 100 AU, the electron densities in the heliosheath ($\sim 0.001\text{--}0.003\text{ cm}^{-3}$) are an order of magnitude smaller than those in the LISM (Gurnett et al. 2013).

Our measurements of electron density for the *Voyager 2* line of sight to GJ

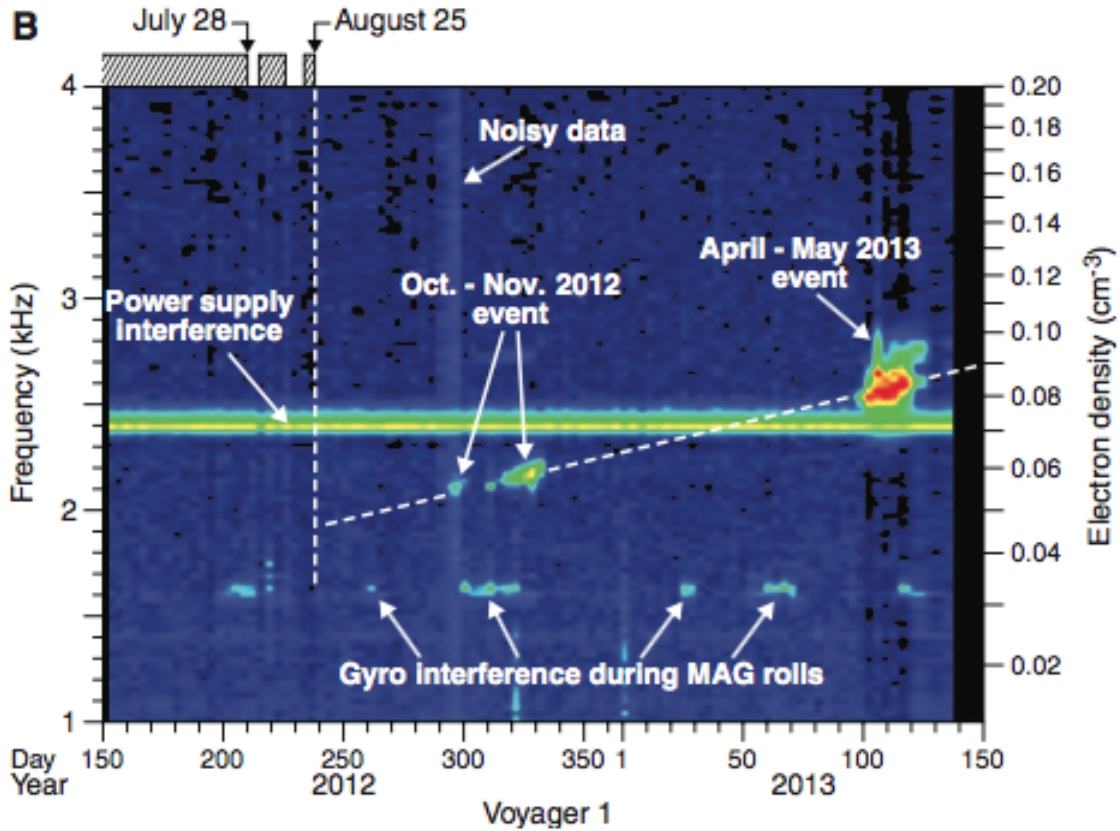


Figure 4.5: A composite spectrogram from Gurnett et al. (2013) that was constructed from spectrograms extending over a 1 year period. Electron density is given in the right-side axis. The vertical dashed white line denotes an increase in galactic cosmic rays in August 2012. The sloping dashed line indicates a density increase in the region between the two marked plasma oscillation events corresponding to an increase of about 19% per AU (Gurnett et al. 2013).

780 clearly indicate the presence of the LISM. The first absorption component, for temperatures between 3110–7000 K, has electron densities between 0.2–0.3 cm^{-3} . Including uncertainties, the electron densities have a total range of 0.05–0.5 cm^{-3} . These values are certainly a factor of three or greater than that measured by *Voyager 1*, but are fairly consistent with previous predictions for electron density in the LISM. The higher densities could suggest the presence of a high-density ISM cloud. Based on our initial comparison to the Redfield & Linsky (2008) Kinematic Model, we can be confident that these higher electron density values confirm the presence of the Vel cloud.

The second absorption component has electron density values between 0.03–0.04 cm^{-3} , which are a factor of three smaller than that measured by *Voyager 1*, but still a full order of magnitude greater than the heliosheath electron density. However, when we calculate an upper limit from the uncertainties, the electron densities range between 0.07–0.1 cm^{-3} , which is both exactly what was measured by *Voyager 1* and predicted by Frisch et al. (2011). Since we believe we see absorption from the Dor cloud, we can conclude that this cloud is less dense than the Vel cloud. Once *Voyager 2* crosses the heliopause within the next five years and obtains new measurements of electron density, we will be able to better compare its measurements with our derived values for electron density.

Chapter 5

Conclusions and Future Work

In June 2016, NASA extended the *Hubble Space Telescope* Science Operations contract to 2021 in the hopes that the telescope would continue to operate until at least 2020.¹ Because it is in low-Earth orbit, *HST* experiences atmospheric drag, and is slowly being pulled back down to Earth. Current estimates on when *Hubble* will succumb to this drag force are sometime between 2030 and 2040. At this point, it is unclear whether or not *HST* will continue to operate during the 2020s until its inevitable destruction. Until then, we can still obtain valuable science data from the telescope. Even with the advent of the *James Webb Space Telescope* era, there is no direct successor to *Hubble* as an ultraviolet and optical space telescope.

Likewise, the *Voyager* spacecraft are expected to fully lose all operational power by 2025,² and will begin to quietly drift through interstellar space. Between the two of them, the *Voyagers* not only explored all four outer planets – Jupiter, Saturn, Uranus, and Neptune – but also investigated 48 moons and the rings and magnetic field systems unique to each planet.³ Spacecraft that were initially built to last only five years have completely exceeded all expectations. When the *Voyagers* do lose power, they will have been traveling for nearly 50 years.

¹<https://www.nasa.gov/press-release/nasa-extends-hubble-space-telescope-science-operations-contract>

²<http://voyager.jpl.nasa.gov/spacecraft/spacecraftlife.html>

³<http://voyager.jpl.nasa.gov/mission/fastfacts.html>

5.1 Future Work

There are several new analyses that can be done to further characterize the LISM near the *Voyager* spacecraft. For example, while complicated, the HI profile contains a substantial amount of information. We can fit the HI absorption by performing a simultaneous fit to both DI and HI absorption. This process follows the same steps as detailed in Section 3, but with a few extra components. In order to better constrain the hydrogen absorption, we fix the centroid velocities of both DI and HI to be equal to each other and utilize the equation, $b(\text{HI}) \approx \sqrt{2}b(\text{DI})$, to set the Doppler parameter widths (Wood et al. 2005). After the first initial run of `gismfit`, the assumed stellar profile (which we presented in Section 3) is altered to refine the overall fit. Since we have assumed the Linsky et al. (2006) D/H value, we can use this to better constrain the HI fit parameters by relating DI to HI. Ultimately, the HI absorption profile becomes more tightly constrained even in the presence of multiple ISM absorption components (Wood et al. 2005).

Figure 5.2 shows the Wood et al. (2005) reconstruction of the stellar Ly α emission line for their target ζ Boo. Each different profile assumes a different column density (between $\log N(\text{HI}) = 17.6\text{--}18.2$). Outside the dashed lines, the profile is estimated based on the assumed $\log N(\text{HI})$, while inside the dashed lines shape is estimated from the shapes of the MgII h and k lines.

Presented in Table 5.1 are the parameters necessary for fully reconstructing the Ly α line of HI in three of four target stars. We will use these column densities, Doppler parameters, and velocities to define the shape of the Ly α continuum emission in the same way as Wood et al. (2005) did. We only list the DI ISM velocities because the HI velocities will be the same. The errors on the HI column densities and b values result from simple error propagation calculations. These parameters

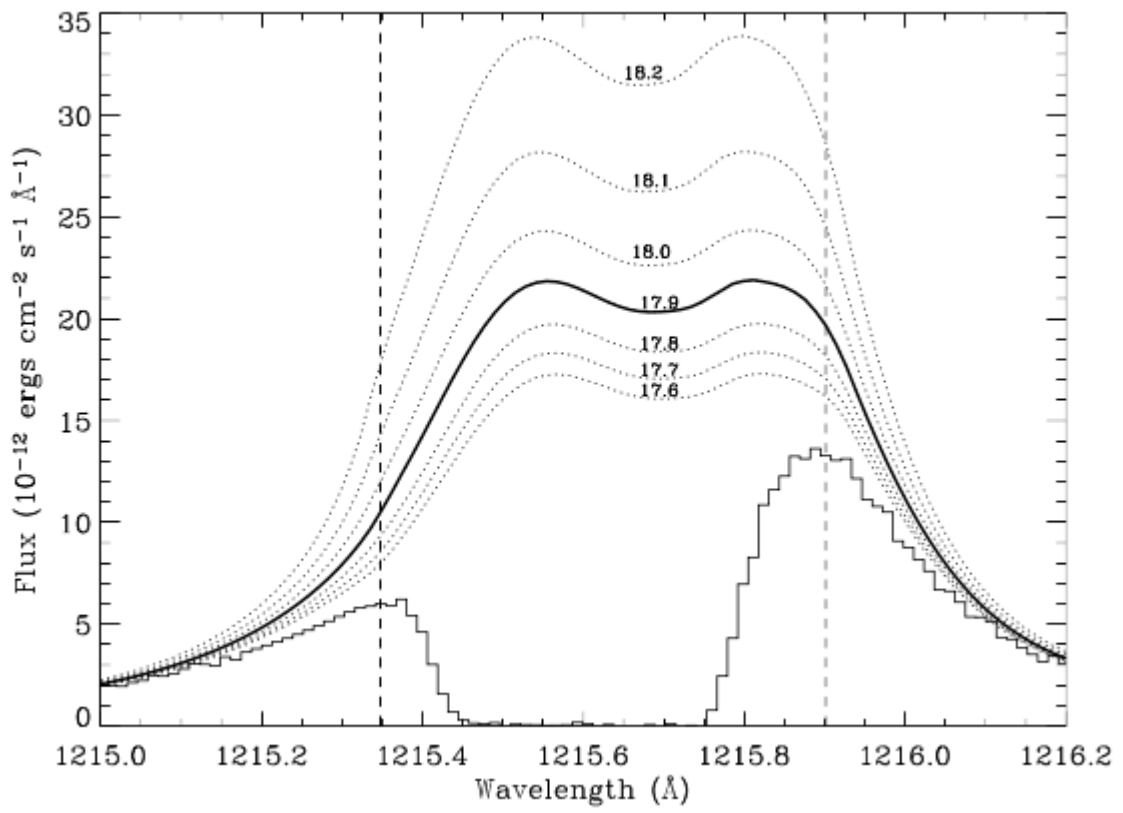


Figure 5.1: A reconstruction of the stellar Ly α line for ζ Boo from Wood et al. (2005).

Table 5.1: Parameters for future reconstruction of the HI Lyman α lines of HIP 85665, GJ 780, and GJ 754.

| Gliese # | Other Name | Component # | v_{DI} (km s $^{-1}$) | b_{DI} (km s $^{-1}$) | b_{HI} (km s $^{-1}$) | $\log N(\text{DI})$ (log cm $^{-2}$) | $\log N(\text{HI})$ (log cm $^{-2}$) |
|------------------|--------------|-------------|------------------------------------|------------------------------------|------------------------------------|--|--|
| <i>Voyager 1</i> | | | | | | | |
| GJ 678.1A | HIP 85665 | 1 | -29.88 ± 0.88 | 7.65 | 10.82 | 13.52 ± 0.09 | 19.33 ± 0.09 |
| | | 2 | -20.3 ± 1.9 | 9.70 | 13.72 | 13.30 ± 0.11 | 19.11 ± 0.11 |
| <i>Voyager 2</i> | | | | | | | |
| GJ 780 | δ Pav | 1 | -16.8 ± 1.6 | 6.0 ± 1.2 | 8.5 ± 1.7 | 12.78 ± 0.25 | 18.59 ± 0.25 |
| | | 2 | -10.4 ± 2.9 | 7.1 ± 1.6 | 10.1 ± 2.2 | 12.85 ± 0.32 | 18.66 ± 0.32 |
| GJ 754 | LHS 60 | 1 | -27.4 ± 2.6 | 5.3 ± 1.3 | 7.4 ± 1.8 | 13.19 ± 0.29 | 19.00 ± 0.29 |
| | | 2 | -18.5 ± 1.2 | 9.47 ± 0.45 | 13.39 ± 0.64 | 13.17 ± 0.10 | 18.98 ± 0.10 |

will be especially important in reconstructing the “wings” of the profile, which we did not do particularly well in the preliminary reconstruction (shown in Figure 3.9). We can see in Figure 5.2 that the amplitude of the Wood et al. (2005) Ly α profile shifts with increasing column density. We predict that the same will apply to our reconstructions. Additionally, we have not yet removed the DI absorption from our Ly α flux data like Wood et al. (2005) did, but we plan on doing so in order for this reconstruction to work. Ultimately, creating and estimating the Lyman α line of HI is tricky business.

Future work may also include acquiring more data on the same targets and looking for new targets. We could obtain more near-UV data with wavelength ranges that include more observable resonance lines. GJ 780 in particular would be a good follow-up target because our current observations yield a high S/N, which would likely be reflected in any subsequent observations. Deviating more than 15° from the *Voyager* sight lines would not characterize their future paths as well, but it would be possible to better characterize that general area of LISM. More distant targets have the disadvantage of being subject to blending, but would help confirm or solidify the results we present in this work.

If we were to acquire more data on the same target stars as used in this work, we could potentially try to obtain a measurement of optical polarization. Polarization has been used to measure the structure of the Local Bubble for column densities $N(\text{H}) > 10^{19.8} \text{ cm}^{-2}$ or distances $< 40 \text{ pc}$ (Frisch et al. 2011). Frisch et al. (2010) obtained interstellar polarization observations of 30 nearby stars within 90° of the heliosphere nose to find the best fits to the polarization position angles. They then compared their results with data from *IBEX*, and found that there was similarity between the polarization direction and that of the *IBEX* Ribbon for the interstellar magnetic field (ISMF). The *IBEX* Ribbon is a band of high energy

neutral atoms that results from charge exchange of interstellar neutrals with protons in the outer heliosphere (Sylla & Fichtner 2015). Optical polarization can therefore provide information about the direction of the local ISMF. Additional comparisons between the ISMF derived from models of the heliosphere (e.g. Zirnstein et al. (2016)) and polarization observations of nearby stars can permit detection of small-scale turbulence. Our four target stars are all within 40 pc and can be considered good targets for follow-up observations at optical wavelengths to look for polarization.

5.2 The “Interstellar Road Map”

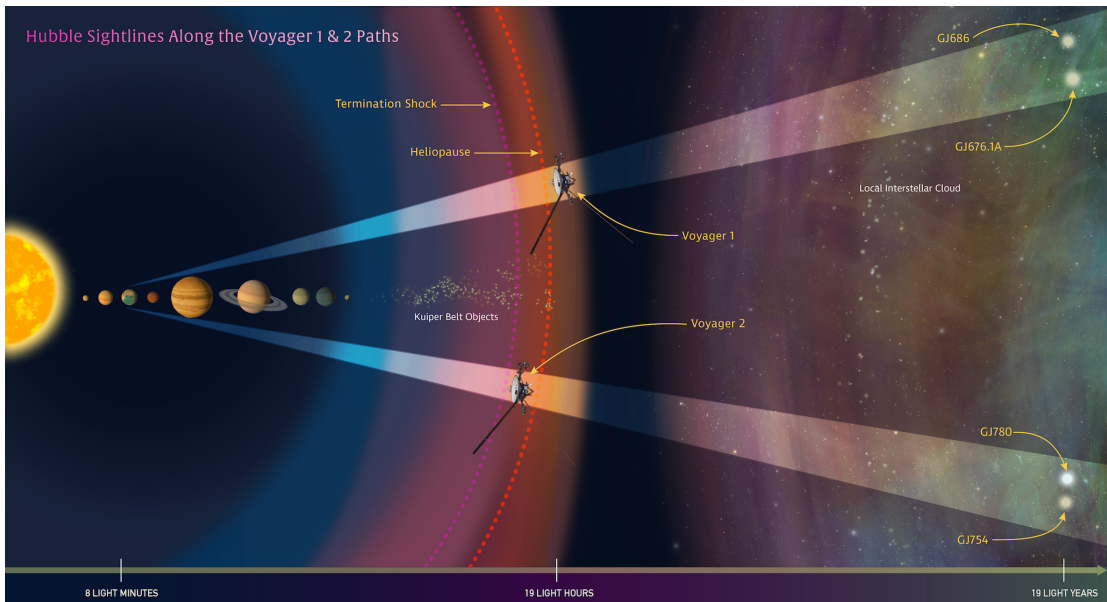


Figure 5.2: An overview of the local ISM, including the two *Voyagers* and their respective sight lines, as well as our four target stars shown on a logarithmic scale. Credit: NASA/STScI.

We have created what we refer to as an “Interstellar Road Map.” We use the *HST* spectra to provide an overview of the ISM along the projected paths of the two *Voyagers*. In the road map analogy, the spectra act as the basis

for the map, providing a general idea of what lies along the path ahead. The *Voyagers* themselves act as the “street view,” sending us valuable measurements of specific local physical properties. The one caveat is that the LISM is a dynamic structure – it is constantly changing and evolving over time. Clouds that are along the *Voyager* lines of sight now may not still be there when, in thousands of years, the spacecraft reach the interstellar space we have probed with *HST*. Figure 5.1 visualizes how our observations directly connect to the *Voyager* spacecraft. Though our target stars are not perfectly along the respective projected *Voyager* lines of sight, they are all within 15° of it.

We have acquired high-resolution spectra along sight lines that canvass the same ISM that the *Voyager* spacecraft are currently measuring, connecting two of NASA’s highly successful and enduring missions. We demonstrate that the local ISM into which the *Voyagers* are moving is a complex and rich environment. Though we observe the closest stars in those directions, we see multiple ISM cloud absorbers. We definitively confirm the presence of known interstellar clouds, including the Local Interstellar Cloud, in three of four sight lines. While some of our comparisons to Redfield & Linsky (2008) do not match up with their derived average values, Redfield & Linsky (2004b) note that variations in temperature and turbulent velocity are common throughout the LISM. This presents the future opportunity to refine the LISM Dynamical Model in the directions of our sight lines. Ultimately, though, we were still able to consider the physical properties of the confirmed clouds. Like *Voyager*, we too measure electron density in the LISM and find that our values match well both with *Voyager* and with the predicted range from Frisch et al. (2011).

The *Voyager* spacecraft each carry a 12-inch gold-plated copper photograph record known as the “Golden Record” containing specific sounds and images that

Tyson stated that the Golden record should be playable for a billion years. Gold on Earth is a naturally-occurring isotope that does not decay atomically, so that the record is gold-plated favors Tyson's conclusion. Additionally, if conditions in the ISM are favorable, the Golden Record does have the potential to survive indefinitely. Therefore, the *Voyager* spacecraft will serve as a sign of humanity's presence in the galaxy in the future.

Both *HST* and the *Voyagers* will be operational for at least the next few years, and so we must consider what additional goals we can accomplish with their remaining capabilities. We have taken observations from two of NASA's longest-enduring and arguably incredibly successful missions and combined them to create an overview of local interstellar space along the paths of the two *Voyager* spacecraft. While this is the first time these missions have been utilized together, hopefully it will not be the last.

Bibliography

- Adams, T. F., & Frisch, P. C. 1977, *ApJ*, 212, 300
- Asplund, M., Grevesse, N., Sauval, A. J., & Scott, P. 2009, *ARA&A*, 47, 481
- Bahcall, J. N., & Wolf, R. A. 1968, *ApJ*, 152, 701
- Blasi, P. 2013, *A&ARv*, 21, 1
- Bonfils, X., et al. 2013, *A&A*, 549, A109
- Bostroem, K. A., & Proffitt, C. 2011, *STIS Data Handbook v. 6.0* (Baltimore: STScI)
- Bristow, P., Kerber, F., & Rosa, M. R. 2006, in *The 2005 HST Calibration Workshop: Hubble After the Transition to Two-Gyro Mode*, ed. A. M. Koekemoer, P. Goudfrooij, & L. L. Dressel, 299
- Burlaga, L. F., & Ness, N. F. 2016, *ApJ*, 829, 134
- Burlaga, L. F., Ness, N. F., Acuna, M. H., Lepping, R. P., Connerney, J. F. P., Stone, E. C., & McDonald, F. B. 2005, *Science*, 309, 2027
- Crutcher, R. M. 1982, *ApJ*, 254, 82
- Draine, B. T. 2009, *SSRv*, 143, 333
- Dyson, J. E., & Williams, D. A. 2003, *The Physics of the Interstellar Medium*, 2nd edn. (Institute of Physics Publishing)

- Evans, D. S. 1967, in IAU Symposium, Vol. 30, Determination of Radial Velocities and their Applications, ed. A. H. Batten & J. F. Heard, 57
- Frisch, P. C., et al. 2010, ApJ, 724, 1473
- . 2009, SSRv, 146, 235
- Frisch, P. C., Grodnicki, L., & Welty, D. E. 2002, ApJ, 574, 834
- Frisch, P. C., Redfield, S., & Slavin, J. D. 2011, ARA&A, 49, 237
- Furlong, R. R., & Wahlquist, E. J. 1999, Nuclear News, 42, 2634
- Gliese, W. 1969, Veroeffentlichungen des Astronomischen Rechen-Instituts Heidelberg, 22
- Goodwin, I., & Cioffi, D. F. 1994, PhT, 47, 42
- Gray, R. O., Corbally, C. J., Garrison, R. F., McFadden, M. T., Bubar, E. J., McGahee, C. E., O'Donoghue, A. A., & Knox, E. R. 2006, AJ, 132, 161
- Grygorczuk, J., Czechowski, A., & Grzedzielski, S. 2015, MNRAS, 450, L76
- Gurnett, D. A., Kurth, W. S., Burlaga, L. F., & Ness, N. F. 2013, Science, 341, 1489
- Jenkins, E. B. 2009, ApJ, 700, 1299
- Jokipii, J. R. 2013, SSRv, 176, 115
- Kimble, R. A., et al. 1998, ApJL, 492, L83
- Koen, C., Kilkenney, D., van Wyk, F., & Marang, F. 2010, MNRAS, 403, 1949
- Kohl, J. L., & Parkinson, W. H. 1976, ApJ, 205, 599

- Kohlhase, C. E., & Penzo, P. A. 1977, *SSRv*, 21, 77
- Krimigis, S. M., Armstrong, T. P., Axford, W. I., Bostrom, C. O., Fan, C. Y., Gloeckler, G., & Lanzerotti, L. J. 1977, *SSRv*, 21, 329
- Krimigis, S. M., Mitchell, D. G., Roelof, E. C., Hsieh, K. C., & McComas, D. J. 2009, *Science*, 326, 971
- Kubiak, M. A., et al. 2014, *ApJS*, 213, 29
- Lépine, S., Hilton, E. J., Mann, A. W., Wilde, M., Rojas-Ayala, B., Cruz, K. L., & Gaidos, E. 2013, *AJ*, 145, 102
- Linsky, J. L., et al. 2006, *ApJ*, 647, 1106
- Linsky, J. L., & Redfield, S. 2014, *Ap&SS*, 354, 29
- Linsky, J. L., Rickett, B. J., & Redfield, S. 2008, *ApJ*, 675, 413
- Linsky, J. L., & Wood, B. E. 1996, *ApJ*, 463, 254
- . 2014, *ASTRA Proceedings*, 1, 43
- Malamut, C., Redfield, S., Linsky, J. L., Wood, B. E., & Ayres, T. R. 2014, *ApJ*, 787, 75
- Maldonado, J., Eiroa, C., Villaver, E., Montesinos, B., & Mora, A. 2015, *A&A*, 579, A20
- Mann, A. W., Feiden, G. A., Gaidos, E., Boyajian, T., & von Braun, K. 2015, *ApJ*, 804, 64
- McComas, D. J., et al. 2012, *Science*, 336, 1291

- . 2015, *ApJS*, 220, 22
- McCray, R., & Snow, Jr., T. P. 1979, *ARA&A*, 17, 213
- Mermilliod, J.-C. 1986, *Catalogue of Eggen's UBV data.*, 0 (1986)
- Metropolis, N., & Ulam, S. 1949, *Journal of the American Statistical Association*, 44, 335
- Mewaldt, R. A., & Liewer, P. C., eds. 2000, *An Interstellar Probe Mission to the Boundaries of the Heliosphere and Nearby Interstellar Space (Space 2000 Conference and Exposition)*
- Möbius, E., et al. 2004, *A&A*, 426, 897
- Morbidelli, A. 2005, *ArXiv Astrophysics e-prints*
- Morton, D. 1991, *ApJS*, 77, 119
- Morton, D. C. 2003, *ApJS*, 149, 205
- Nidever, D. L., Marcy, G. W., Butler, R. P., Fischer, D. A., & Vogt, S. S. 2002, *ApJS*, 141, 503
- Nussbaumer, H., & Storey, P. J. 1981, *A&A*, 96, 91
- Oort, J. H. 1950, *Bull. Astron. Inst. Netherlands*, 11, 91
- Opher, M., Bibi, F. A., Toth, G., Richardson, J. D., Izmodenov, V. V., & Gombosi, T. I. 2009, *Nature*, 462, 1036
- Opher, M., Stone, E. C., & Liewer, P. C. 2006, *ApJL*, 640, L71
- Owens, M. J., & Forsyth, R. J. 2013, *Living Rev. Sol. Phys.*, 10

- Parker, E. N. 1958, *ApJ*, 128, 664
- Phillips, N. M., Greaves, J. S., Dent, W. R. F., Matthews, B. C., Holland, W. S., Wyatt, M. C., & Sibthorpe, B. 2010, *MNRAS*, 403, 1089
- Redfield, S., & Falcon, R. E. 2008, *ApJ*, 683, 207
- Redfield, S., & Linsky, J. L. 2002, *ApJS*, 139, 439
- . 2004a, *ApJ*, 602, 776
- . 2004b, *ApJ*, 613, 1004
- . 2008, *ApJ*, 673, 283
- . 2015, *ApJ*, 812, 125
- Richardson, J. D., Liu, Y., & Wang, C. 2008, *AdSpR*, 41, 237
- Robberto, M., Sivaramakrishnan, A., Bacinski, J. J., Calzetti, D., Krist, J. E., MacKenty, J. W., Piquero, J., & Stiavelli, M. 2000, in *Proceedings of SPIE*, Vol. 4013, *UV, Optical, and IR Space Telescopes and Instruments*, ed. J. B. Breckinridge & P. Jakobsen, 386–393
- Rodgers, A. W., & Eggen, O. J. 1974, *PASP*, 86, 742
- Rudd, R. P., Hall, J. C., & Spradlin, G. 1997, *AcAau*, 40, 383
- Sagan, C. 1994, *Pale Blue Dot: A Vision of Human Future in Space* (Random House)
- Savage, B. D., & Sembach, K. R. 1996, *ARA&A*, 34, 279
- Scarf, F. L., & Gurnett, D. A. 1977, *SSRv*, 21, 289

- Schultz, C. 2014, EOS Transactions, American Geophysical Union, 95, 388
- Schwadron, N. A., Richardson, J. D., Burlaga, L. F., McComas, J. D., & Möbius, E. 2015, ApJL, 813, L20
- Shayler, D. J., & Harland, D. M. 2016, The Hubble Space Telescope: From Concept to Success (Praxis)
- Sousa, S. G., et al. 2008, A&A, 487, 373
- Sparavigna, A. C., & Marazzato, R. 2010, ArXiv e-prints
- Stone, E. C., Alkalai, L., & Friedman, L. 2014, in Keck Institute for Space Studies
- Stone, E. C., Richardson, J. D., Angrum, A., & Massey, E. B. 2005, Voyager Interstellar Mission: Proposal to Senior Review 2005 of the Mission Operations and Data Analysis Program for the Sun-Solar System Connection Operating Missions
- Stone, E. C., Vogt, R. E., McDonald, F. B., Teegarden, B. J., Trainor, J. H., Jokipii, J., & Webber, W. 1977, SSRv, 21, 355
- Sylla, A., & Fichtner, H. 2015, ApJ, 811, 150
- Takeda, G., Ford, E. B., Sills, A., Rasio, F. A., Fischer, D. A., & Valenti, J. A. 2007, ApJS, 168, 297
- van Leeuwen, F. 2007, A&A, 474, 653
- Webber, W. R., & McDonald, F. B. 2013, GeoRL, 40, 1665
- Witte, M. 2004, A&A, 426, 835

- Wood, B. E., Redfield, S., Linsky, J. L., Müller, H. R., & Zank, G. P. 2005, *ApJS*, 159, 118
- Wood, B. E., Redfield, S., Linsky, J. L., & Sahu, M. S. 2002, *ApJ*, 581, 1168
- Woodgate, B. E., et al. 1998, *PASP*, 110, 1183
- Xapsos, M. A., et al. 2014, *ITNS*, 61, 3356
- Zacharias, N., Finch, C. T., Girard, T. M., Henden, A., Bartlett, J. L., Monet, D. G., & Zacharias, M. I. 2012, *VizieR Online Data Catalog*, 1322
- Zank, G. P., Heerikhuisen, J., Wood, B. E., Pogorelov, N. V., Zirnststein, E., & McComas, D. J. 2013, *ApJ*, 763, 20
- Zirnststein, E. J., Heerikhuisen, J., Funsten, H. O., Livadiotis, G., McComas, D. J., & Pogorelov, N. V. 2016, *ApJL*, 818, L18